

CONTRACTOR REPORT

SAND89-7029
Unlimited Release
UC-275



8232-2/069226



00000001 -

8524
RS-8232-2/69226

cy!

Use of Imaging Refractive Secondaries in Photovoltaic Concentrators

Dr. Lawrence W. James
James Associates
1525 East County Road 58
Fort Collins, CO 80524

Prepared by Sandia National Laboratories Albuquerque, New Mexico 87185
and Livermore, California 94550 for the United States Department of Energy
under Contract DE-AC04-76DP00789

Printed July 1989

NC

Issued by Sandia National Laboratories, operated for the United States Department of Energy by Sandia Corporation.

NOTICE: This report was prepared as an account of work sponsored by an agency of the United States Government. Neither the United States Government nor any agency thereof, nor any of their employees, nor any of their contractors, subcontractors, or their employees, makes any warranty, express or implied, or assumes any legal liability or responsibility for the accuracy, completeness, or usefulness of any information, apparatus, product or process disclosed, or represents that its use would not infringe privately owned rights. Reference herein to any specific commercial product, process, or service by trade name, trademark, manufacturer, or otherwise, does not necessarily constitute or imply its endorsement, recommendation, or favoring by the United States Government, any agency thereof or any of their contractors or subcontractors. The views and opinions expressed herein do not necessarily state or reflect those of the United States Government, any agency thereof or any of their contractors.

Printed in the United States of America. This report has been reproduced directly from the best available copy.

Available to DOE and DOE contractors from
Office of Scientific and Technical Information
PO Box 62
Oak Ridge, TN 37831

Prices available from (615) 576-8401, FTS 626-8401

Available to the public from
National Technical Information Service
US Department of Commerce
5285 Port Royal Rd
Springfield, VA 22161

NTIS price codes
Printed copy: A04
Microfiche copy: A01

SAND89-7029
Unlimited Release
Printed July 1989

USE OF IMAGING REFRACTIVE SECONDARIES IN PHOTOVOLTAIC CONCENTRATORS

Dr. Lawrence W. James
James Associates
1525 East County Road 58
Fort Collins, CO 80524
303-484-5296

Sandia Contract 05-8713

ABSTRACT

A new type of secondary optical element for two-axis photovoltaic solar concentrator systems is described. This optical system is known as the double-imaging concentrator system because the sun is imaged by the primary Fresnel lens onto the secondary lens, and the primary lens is imaged by the secondary lens onto the cell. The secondary lens can take two forms. An egg-shaped (ellipsoidal) glass secondary is suspended above the cell in one implementation. The alternative configuration, called the SILO secondary, allows gluing the secondary lens directly to the cell. This SILO lens is a glass cylinder or cone with a molded half-ellipsoidal top surface. In both cases, the fact that the primary lens is imaged onto the cell means that if the primary lens is uniformly illuminated, then the cell is uniformly illuminated, independent of first-order of tracking errors, mounting errors, and primary Fresnel lens aberrations. Monte Carlo ray trace modeling of these systems with the "FgImgSec" computer code shows significant advantages over other optical systems in the important areas of photon flux uniformity over the solar cell surface, and maximum allowable mounting and aiming tolerances. Parametric studies of concentration ratio and primary lens f-number show the limits in system design and give guidance for system optimization.

ACKNOWLEDGEMENTS

This work originated from a crude experimental optical model built by Jacques Ludman of Photics, Inc. that showed the use of a compensating lens to reduce tracking error sensitivity. This contract follows up work by James Associates on earlier Sandia and EPRI contracts where the concept was initially investigated. Thanks to Charlie Stillwell and others at Sandia for helpful suggestions which were incorporated into this report.

TABLE OF CONTENTS

<u>SECTION</u>	<u>PAGE</u>
Limitations of Currently Used Secondaries	1
Double Imaging Concentrating Optics	3
The Single Surface Imaging Secondary	19
System Design Considerations	33
Properties of Glass Appropriate for an Imaging Secondary	39
Operation of the SILO Secondary at other than the Focal Point	43
Conclusions	49

LIST OF FIGURES

<u>SECTION</u>	<u>PAGE</u>
Figure 1: Example of a Double Imaging Concentrator.	3
Figure 2: Ray traces showing origination points on the primary Fresnel lens.	4
Figure 3: Ray traces showing the imaging properties of the secondary lens.	5
Figure 4: Spot diagram showing the imaging properties of the lens.	6
Figure 5: Monte Carlo ray trace spot patterns for the 300X egg secondary.	8
Figure 6: Short-circuit current flux for the cell in the 300X egg secondary.	9
Figure 7: Optical transmission vs. tracking error in the 300X egg secondary.	10
Figure 8: Peak flux density vs. tracking error in the 300X egg secondary.	11
Figure 9: Optical transmission with a single layer AR coating.	12
Figure 10: Optical transmission with no AR coating.	13
Figure 11: Optical transmission vs. mounting error in the cell plane.	14
Figure 12: Peak flux density vs. mounting error in the cell plane.	15
Figure 13: Optical transmission vs. mounting error perpendicular to the cell plane.	16
Figure 14: Peak flux density vs. mounting error perpendicular to the cell plane.	17
Figure 15: Example of a single surface imaging secondary concentrator.	19
Figure 16: Close up of the secondary lens and cell assembly in a SILO design.	20
Figure 17: The SILO optical system used for modeling.	21
Figure 18: Close up of a SILO cell assembly showing the imaging properties.	22
Figure 19: Spot diagram showing the imaging properties of the SILO secondary.	23
Figure 20: Monte Carlo ray trace spot patterns for the 300X SILO secondary.	24
Figure 21: Short-circuit current flux for the cell in the 300X SILO secondary.	25
Figure 22: Optical transmission vs. tracking error in the 300X SILO secondary.	26
Figure 23: Peak flux density vs. tracking error in the 300X SILO secondary.	27
Figure 24: Optical transmission vs. tracking error with a single layer AR coating.	28
Figure 25: Peak solar flux vs. tracking error with a single layer AR coating.	29
Figure 26: Optical transmission vs. tracking error with no AR coating.	30
Figure 27: Peak solar flux vs. tracking error with no AR coating.	31
Figure 28: Comparison of an egg secondary with a SILO secondary.	32
Figure 29: Transmission of a 600X SILO system versus primary lens F#.	33
Figure 30: Transmission of a 300X SILO system versus primary lens F#.	34
Figure 31: Transmission of a 1000X SILO system versus primary lens F#.	35
Figure 32: Transmission of a 3000X SILO system versus primary lens F#.	36
Figure 33: Obtainable geometric concentrations.	37
Figure 34: Solar flux density in the middle of a SILO secondary element.	39
Figure 35: Optics transmission vs. tracking error for three different glasses.	40
Figure 36: Three different glasses near the 0 tracking error point.	41
Figure 37: Optical transmission vs. secondary glass infrared absorption coefficient.	42
Figure 38: Close-up of a SILO cell assembly showing the imaging properties.	43
Figure 39: Close-up of a SILO cell assembly with an enlarged secondary.	44
Figure 40: Spot diagram showing the ray bundles on the cell.	45
Figure 41: Cell short-circuit current flux in the 300X enlarged secondary example.	46
Figure 42: Comparison of an on-focus to a beyond-focus SILO secondary.	47
Figure 43: Peak solar flux of the beyond-focus optical system versus tracking error.	48
Figure 44: Flux uniformity under a combination of error conditions.	49

Limitations of Currently Used Secondaries

Current designs for concentrator photovoltaic systems use either a hollow reflective metal cone secondary or a solid glass cone secondary that relies on total internal reflection (TIR). Each of these types of secondaries has several disadvantages.

With an aluminum cone secondary, the cell surface is exposed to the atmosphere. The cell may require a protective covering to achieve high reliability over a long operating life. This covering is an additional expense and may cause additional optical losses due to reflectivity from its front surface. The measured reflectivity of real aluminum secondaries is less than the theoretical reflectivity for aluminum and is considerably less than 1, causing serious optical losses, especially under off-track conditions.

TIR secondaries, to be economically attractive, would need to be produced by some sort of molding process. Glass molding can produce high-quality surfaces, but cannot produce sharp corners. The TIR secondary requires sharp corners next to the cell to prevent serious optical losses. The TIR secondary must be glued to the cell with a flexible optical cement, but the cement must not be allowed to touch the side of the secondary. The manufacturing and assembly processes have such tight tolerances that they may never be cost effective.

The Fresnel primary lens design for either of these types of secondaries is a compromise done by trying to juggle ray placement to reduce optical losses and keep the peak flux on the cell from becoming excessive. The optimum design depends on the grid pattern of the cell. However the juggling is done, it is a delicate balancing act of rays from different zones on the lens, of rays bounced and not bounced off of the secondary, etc. That delicate balance disappears rapidly when the Fresnel lens warps due to humidity, or a tracking or mounting error occurs, forcing up the cost of the system by requiring fairly tight tolerances and material thicknesses, weights, and prices determined by stiffness criteria. A cone secondary of optimum optical design may be too expensive, forcing further efficiency losses due to economics. No designer can ever be sure of having the "best" design of this type, regardless of how much time was spent trying different lens zoning schemes.

An ideal secondary optical element would circumvent these limitations. It would give a uniform flux distribution over the cell while incurring minimal optical losses. The flux distribution it produced on the cell would be much less sensitive to tracking and mounting errors, allowing a loosening of system tolerances. Its design would be straightforward and would not involve any precise balancing of ray placement by Fresnel-facet-angle fine-tuning. It would be mechanically rugged, would protect the cell surface from moisture and corrosion, would deliver high optical efficiency, and would be economical to produce in a high-volume, vertically integrated manufacturing operation. Fortunately there is such a secondary. The purpose of this report is to detail its design and use.

The calculations and figures shown in this report were all done by computer simulation using the ray tracing software "FgImgSec" (Flat groove Imaging Secondary), which is available from James Associates for HP 9000 computers and PC compatibles. No actual hardware was constructed on this contract, and all results shown are calculations rather than experimental measurements.

Double Imaging Concentrating Optics

The best optical system, at the current state of the art, for solar concentration in the 200-500X range onto photovoltaic cells is the double imaging system. It consists of two lenses, a Fresnel primary lens, which images the sun onto the middle of the secondary lens, and a solid aspheric secondary lens, which images the primary lens onto the cell¹. Figure 1 below shows an overview of the optical system, with the Fresnel primary lens on the left, the cell on the right, and the secondary lens between the two, close to the cell.

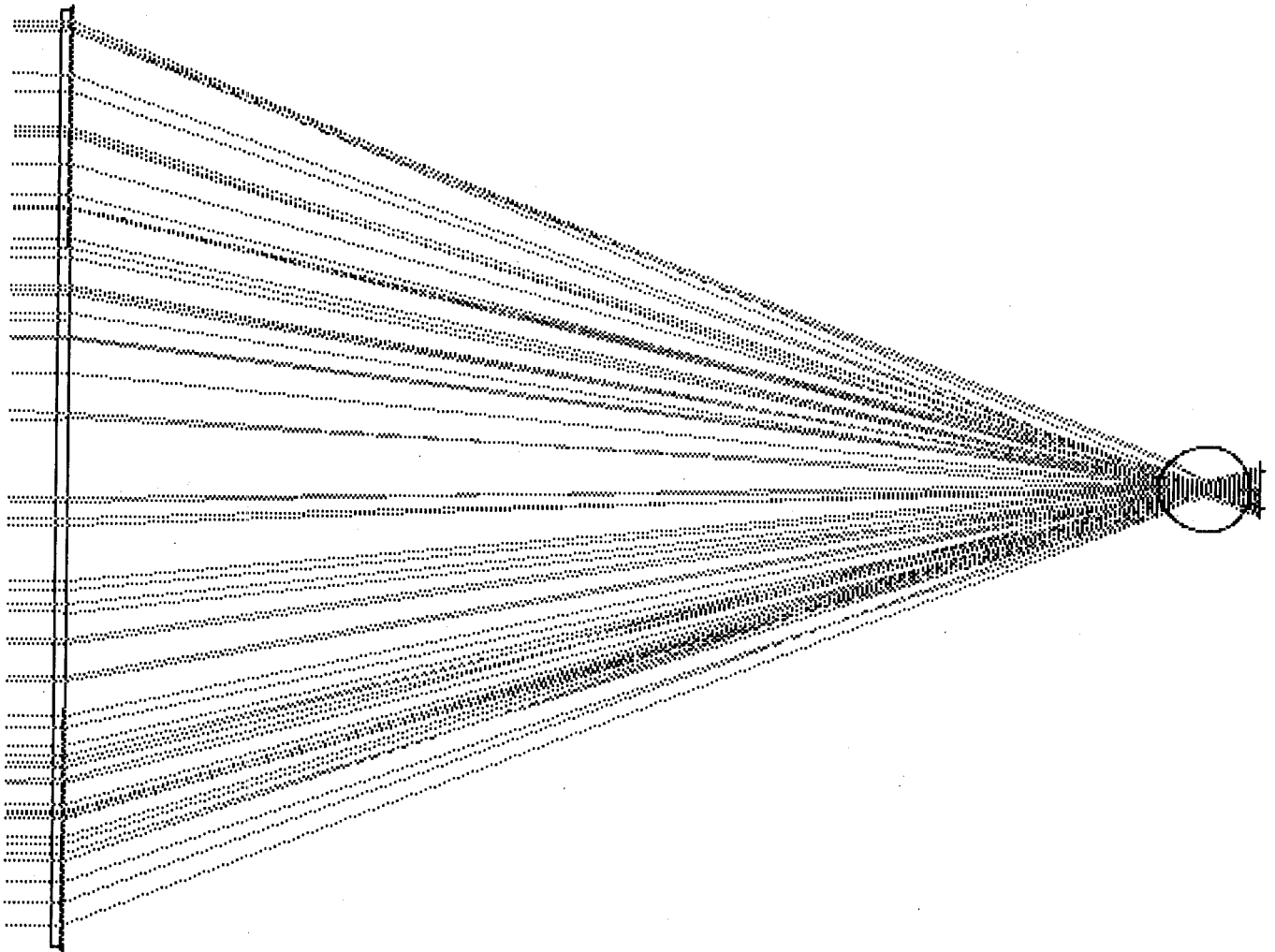


Figure 1: Example of a double imaging concentrator.

The Fresnel lens is designed as an imaging lens, placing an image of the sun in the plane of the widest part of the secondary lens. This makes the Fresnel lens straightforward to design. In aiming as much of the light as possible as close to the center of the secondary as possible, it also gives the widest possible tolerances for tracking and mounting errors.

¹ Aden B. Meinel and Marjorie P. Meinel, Applied Solar Energy, An Introduction (Reading, Massachusetts: Addison-Wesley Publishing Company, 1976), p. 192.

Figure 2 shows the Fresnel lens (along its diagonal), the secondary lens and the cell with light incident at three discrete points on the primary lens (the center, the corner, and the center to edge distance), so that the imaging of points on the Fresnel lens may be seen in the traced rays.

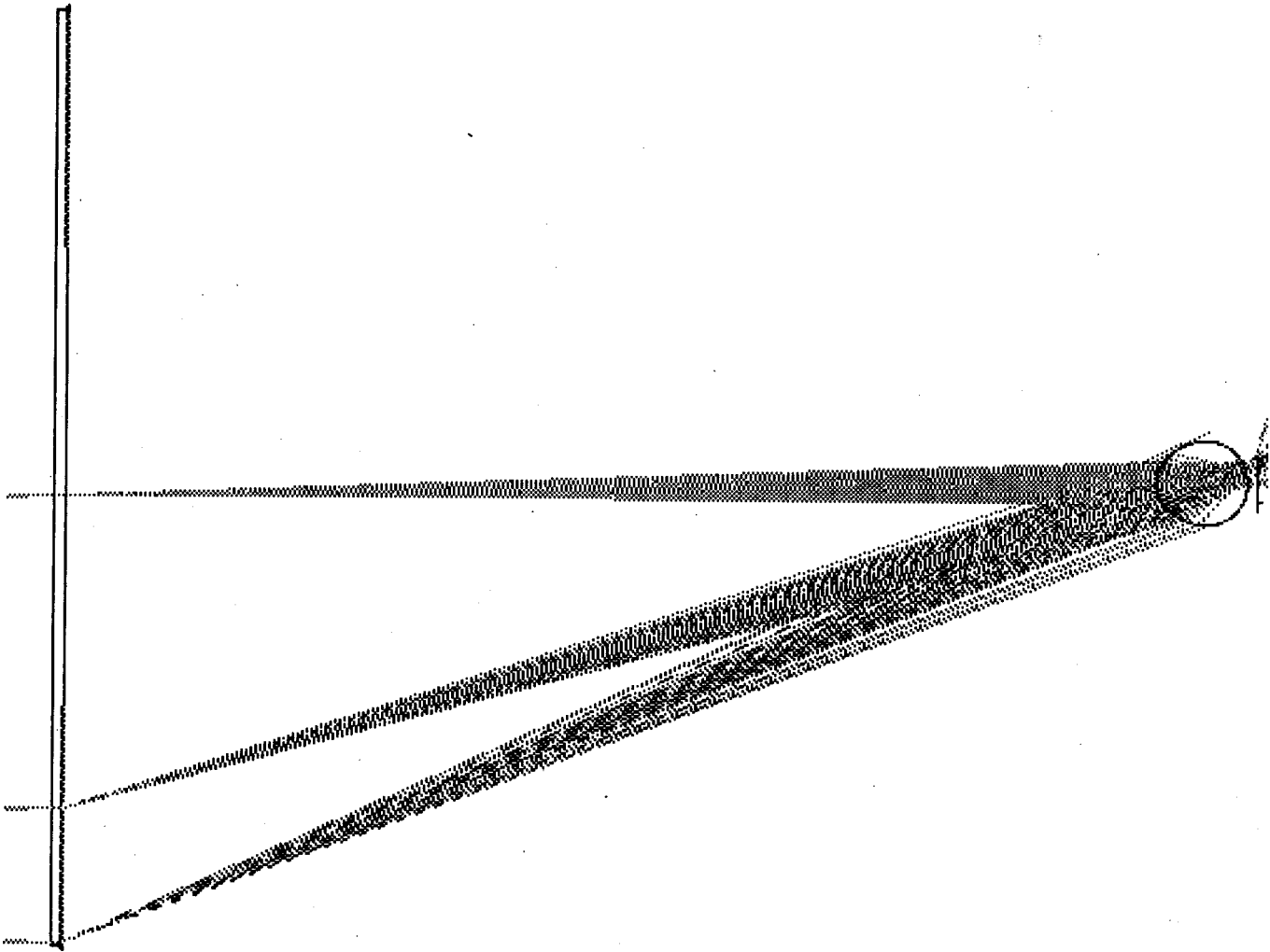


Figure 2: Ray traces showing origination points on the primary Fresnel lens.

Figure 3 shows a close-up of the secondary lens and the cell (along its diagonal) for the case in which light is incident at the three discrete points on the primary lens, points that are shown in Figure 2. Each point on the Fresnel primary lens is imaged to a point on the cell.

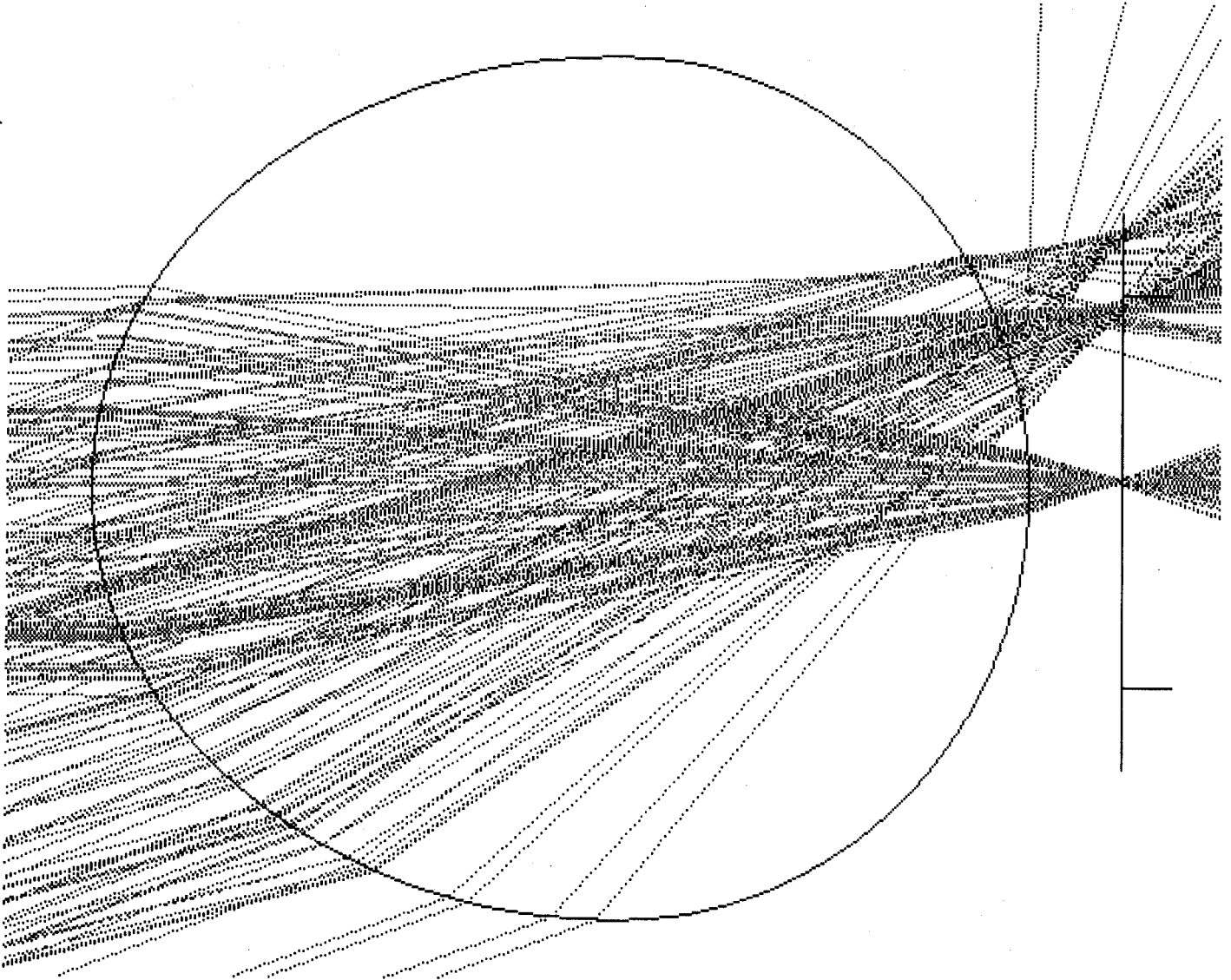


Figure 3: Ray traces showing the imaging properties of the secondary lens.

This secondary lens may be understood by an analogy to a camera lens. The secondary lens essentially takes a picture of the primary lens onto the cell, which is where the film would be in a camera. The secondary lens is very fast, with an effective f -number of approximately 0.6 so that it is an efficient light collector. As such, it must be made in an aspheric shape to perform well.

The secondary lens would probably be manufactured by a molding process, so the aspheric shape should not be an additional cost element for each manufactured lens, only for the original tooling. The lens could be made from moldable optical glass as is done by several manufacturers for similar lenses used in other fields (such as disposable cameras and condenser lenses). It might even be possible to mold the lens in plastic, although the high solar flux densities present in the lens could limit this option.

Figure 4 shows ray spot patterns on the lens, the secondary input, and the cell, for an enlarged artificial sun (to represent many different tracking errors at once) with an angular diameter of 2.17° (instead of 0.54°), and for discrete points laid out in a rectangular array on the lens surface. The scatter in the dots on the cell plane shows the accuracy of imaging that is obtained. It is not perfect, but it is quite adequate for this application.

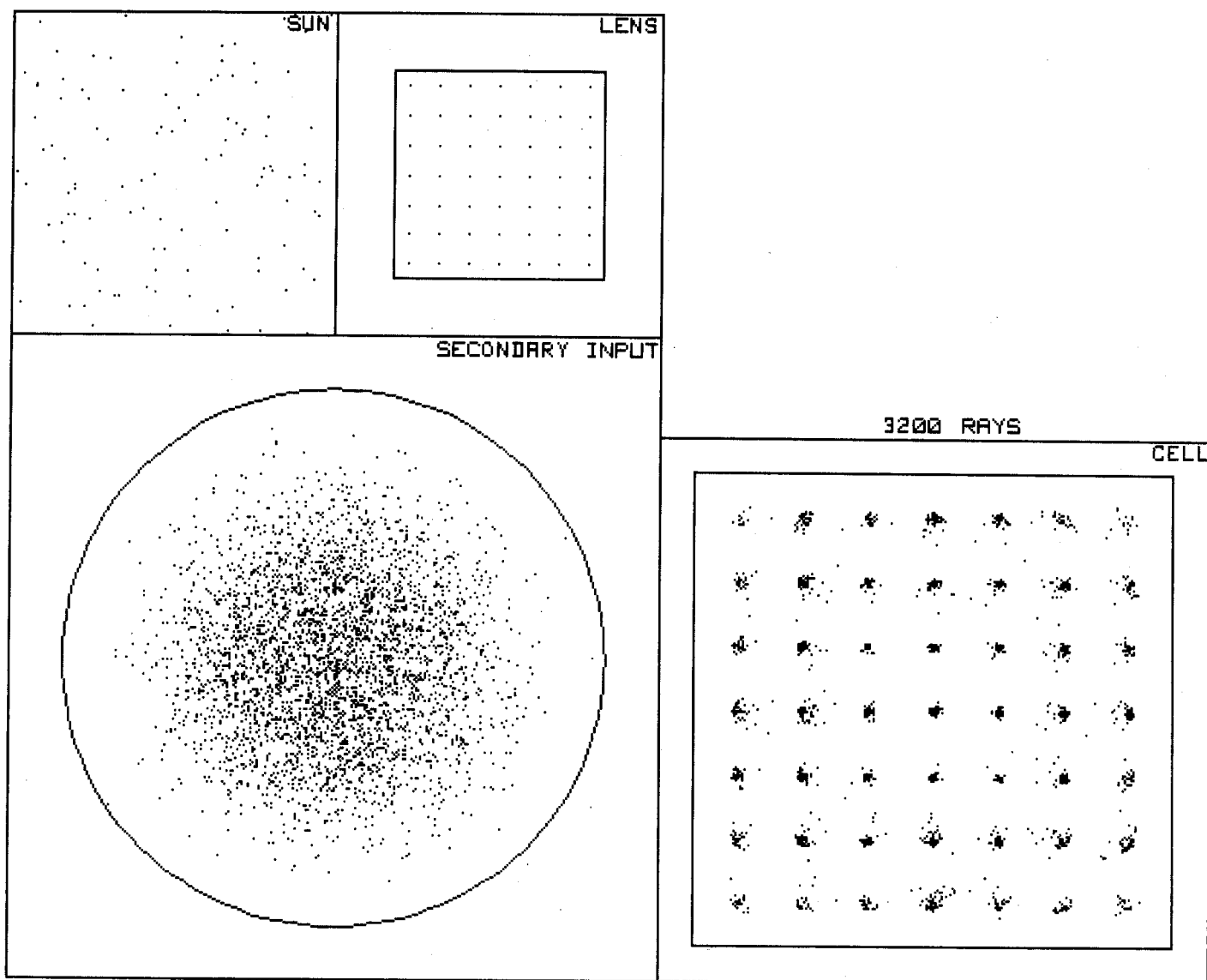


Figure 4: Spot diagram showing the imaging properties of the lens.

Forming an image of the Fresnel lens on the cell has several advantages. If the Fresnel lens is uniformly illuminated, then the cell is uniformly illuminated, independent of the exact direction of the rays coming out of the Fresnel lens. This means that (to first order) when the array is off track or the Fresnel lens becomes dome shaped because of moisture, the flux distribution on the cell doesn't change.

The chromatic aberration of the primary lens is corrected by the secondary lens, making the cell illumination not only very uniform in total flux, but also in flux at each individual wavelength. One would not have to change the design to switch between Si and GaAs cells.

A reduction in image size occurs in the imaging process, just as in a camera. In the case of a 300X concentrator system, the width of the lens image on the cell is about $1/\sqrt{300} = 5.8\%$ of the actual lens width. If you think about the imaging process, you will realize that the primary lens may be offset from the secondary-cell assembly in the X-Y plane by a significant amount, while only shifting the image on the cell by 5.8% of that amount. This makes the system very tolerant of X-Y plane mounting errors between the primary lens and the secondary lens-cell assembly.

The system is also very tolerant of mounting errors in Fresnel-lens to cell-assembly spacing. Changing this spacing simply moves the image on the cell out of focus slightly. The allowable error range of Fresnel-lens to cell-assembly spacing may be compared to the depth-of-field range of a camera.

All of these discussions of insensitivity to all sorts of tolerances only apply, of course, as long as the rays from the primary lens actually hit the secondary lens. That is why the Fresnel lens is designed to direct its rays to the center of the secondary lens. Examination of Figure 1 shows that (depending on the mounting scheme for the secondary) some rays that miss the secondary under extreme error conditions may hit the cell directly.

Moving now from generalities to specifics, we look at the calculated performance at air mass 1.5 of a specific example design of a 300X geometric concentrator of this type. The cell is square, the primary Fresnel lens is a 7-inch square compression-molded lens with 0.06-inch wide facets, and the lens-to-cell spacing is 12.518 inches. The secondary is molded out of BK7 glass. The secondary looks like an egg and is composed of half of an ellipsoid on the top and half of a ellipsoid with a different major axis on the bottom. The secondary lens has a diameter of 0.890 inches. Thus each ellipsoidal surface has a minor axis of 0.890 inches. The major axis of the upper ellipsoid is 1.077 inches. The major axis of the lower ellipsoid is 0.845 inches. The widest point in the secondary is mounted 0.518 inches above the cell top surface, giving a clearance of 0.096 inches between the secondary bottom and the cell.

While the computer graphics show the lens as a smooth-surfaced egg, in manufacturing by molding, there would be a "belt" about 0.05 inches wide around the middle of the egg where the glass was squeezed out in between the top and bottom halves of the mold. The upper flat surface of this belt would be used as the mounting surface for the secondary lens. (The upper surface is used so that molding tolerances in the belt width do not affect the most critical dimension in the assembly, which is the top-lens-surface to cell-plane distance).

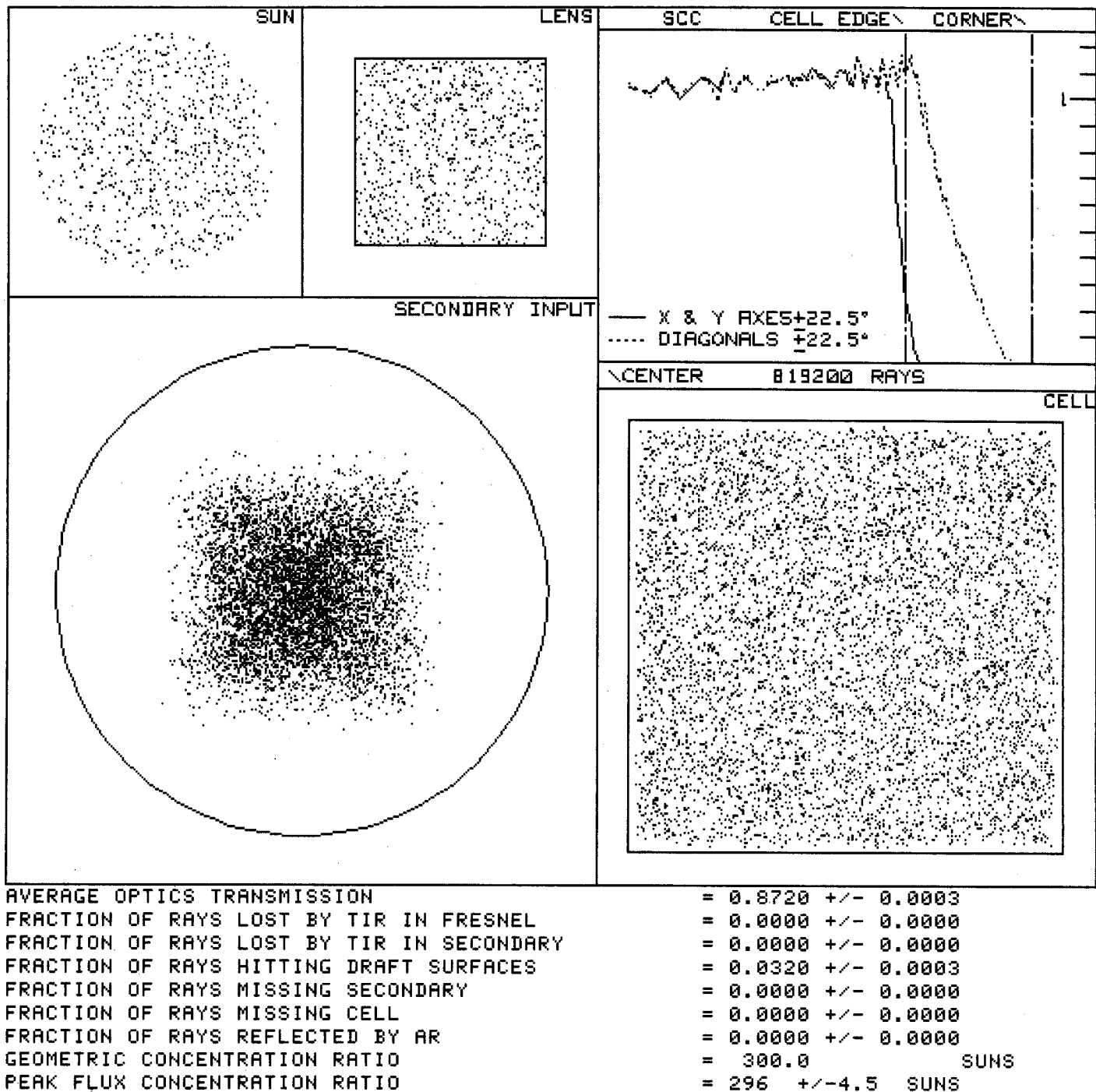


Figure 5: Monte Carlo ray trace spot patterns for the 300X egg-shaped secondary example.

The computer printout in Figure 5 shows the ray spot patterns for this design when everything is in perfect alignment. Note that there is an unilluminated band 0.007-inch wide around the edge of the cell active area. This is to provide a ± 0.005 -inch tolerance for mounting of the center of the secondary lens with respect to the center of the cell. These values plus the ± 0.005 -inch tolerance for the distance from the top of the secondary-lens-mounting-belt to the cell plane are the only two dimensions in the entire module that must be held to close tolerances.

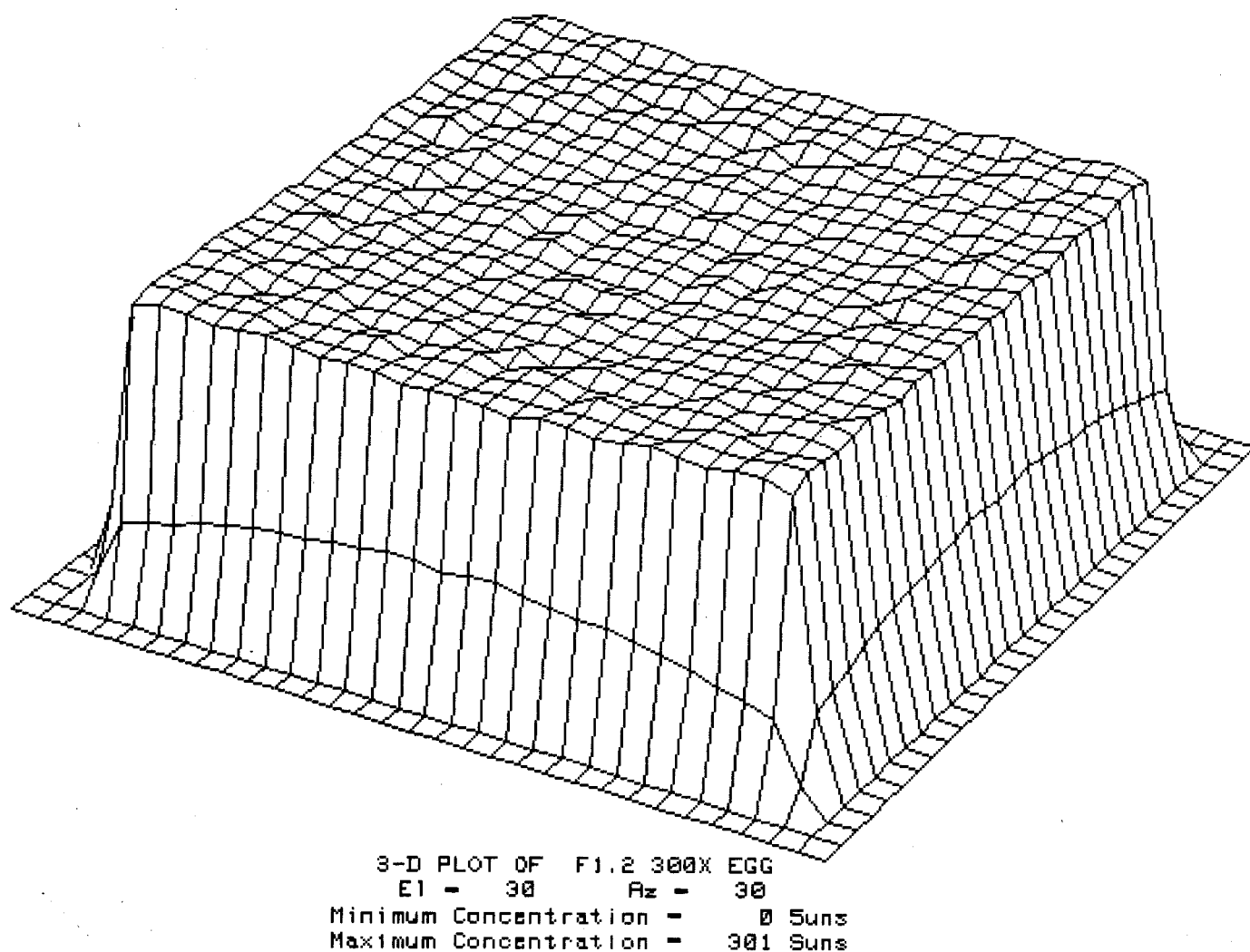


Figure 6: Short-circuit current flux for the cell in the 300X egg-shaped secondary example.

Variation in short-circuit current flux over the active area of the cell is shown in Figure 6. The cell occupies all but the outer row of squares in the figure. Note that the flux is extremely uniform. Such a uniform flux should eliminate the loss in cell performance caused by nonuniform illumination. High-resistivity cells have a loss in performance when the incident flux is nonuniform due to lifetime shortening from high carrier concentrations in the high-flux regions. Low-resistivity cells have a loss in performance when the incident flux is nonuniform due to increased IR losses in the grid lines and the semiconductor sheet resistivity.

The high transmission and uniform flux without spillage off the sides of the cell are preserved with tracking and mounting errors that would occur in a real system, not just with everything modeled to be in perfect alignment. Figure 7 shows the optics transmission versus tracking error. It is virtually flat out to 0.7 degree and quite usable out to a full 1.2 degrees tracking error.

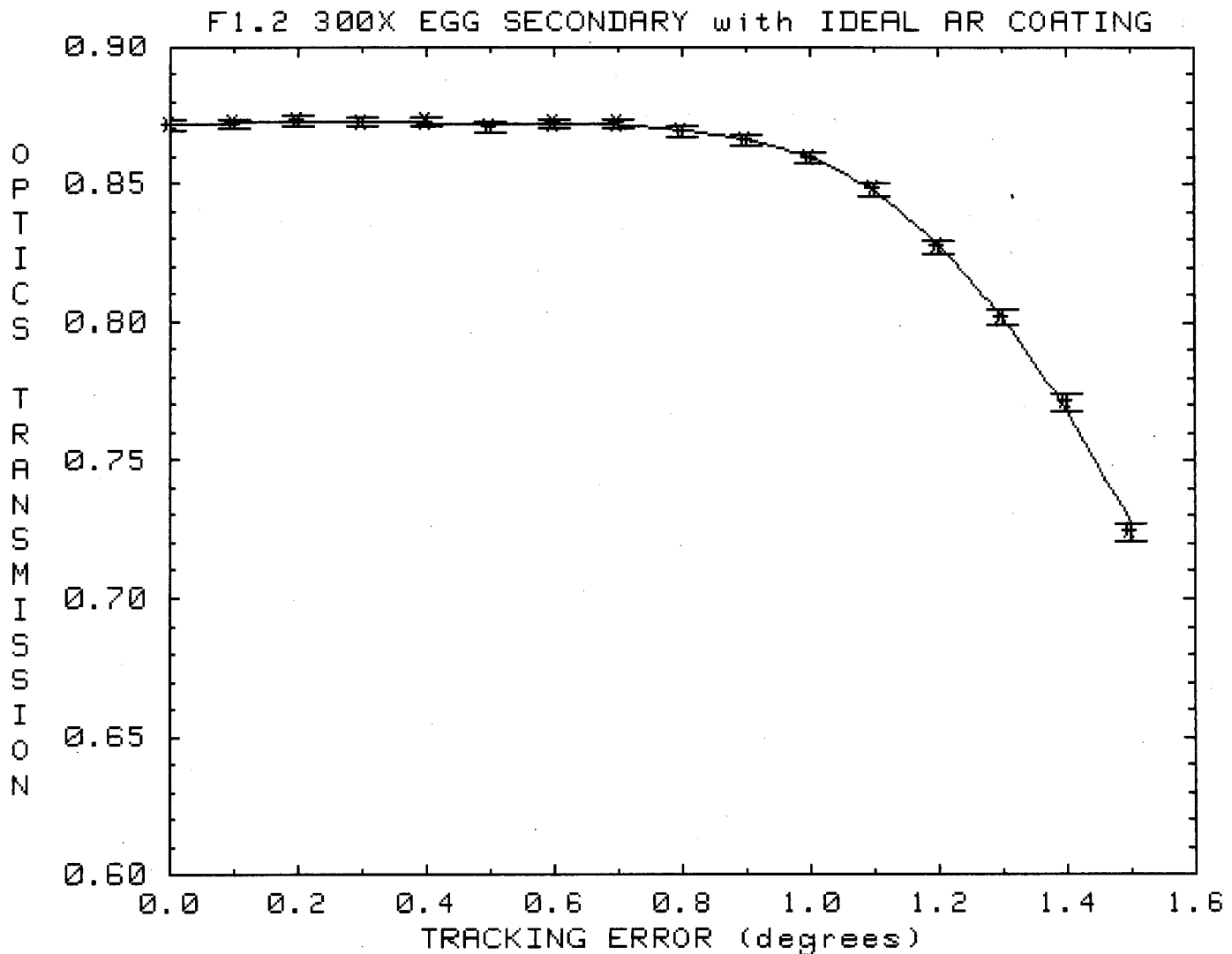


Figure 7: Optical transmission (short-circuit current weighted) of the complete optical system versus tracking error in the 300X egg-shaped secondary example.

The peak flux occurring on the cell gives a good indication of how uniform the flux distribution stays. Figure 8 shows that the peak flux remains at a nearly constant 300 suns out to 0.9-degree tracking error, and only reaches 450 suns under worst case tracking error conditions.

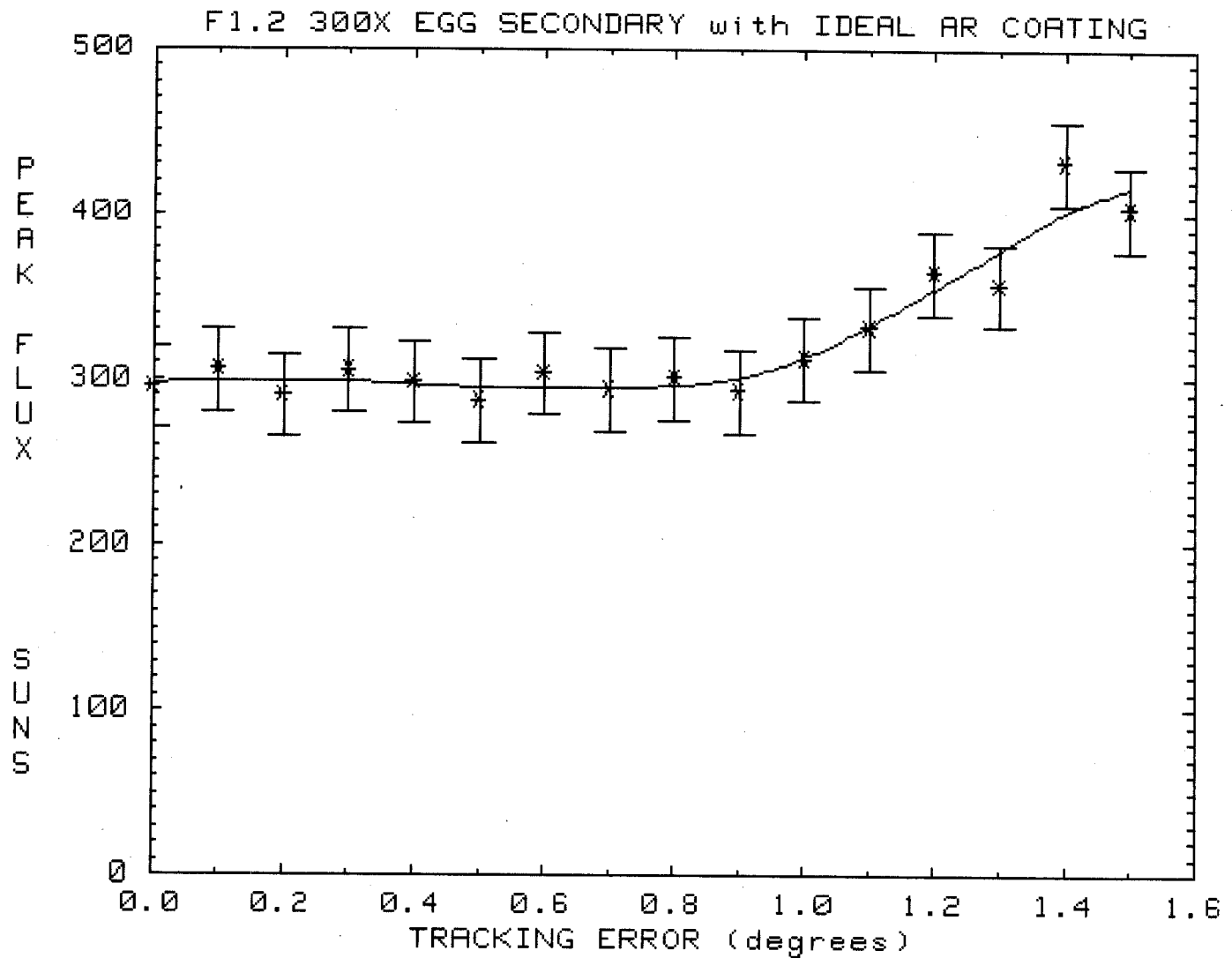


Figure 8: Peak flux density (short-circuit current weighted) of the complete optical system versus tracking error in the 300X egg-shaped secondary example.

The curves shown so far have been for an ideal multi-layer antireflection (AR) coating applied to the secondary lens. Such a coating would minimize reflective losses at the two secondary surfaces. These coatings are common practice in the camera industry, but may not be economically viable for solar systems without some breakthrough in thin film deposition technology.

The same curves were calculated for a single layer AR coating of a material such as MgF. Such a single layer AR coating may be economically viable, especially if it can be done by a chemical dip or spray of the secondary lens. The transmission curve for that case is shown in Figure 9. The fall off in transmission below 0.8 degrees tracking error is principally due to increasing reflectivity of the secondary lens with an oblique incidence angle.

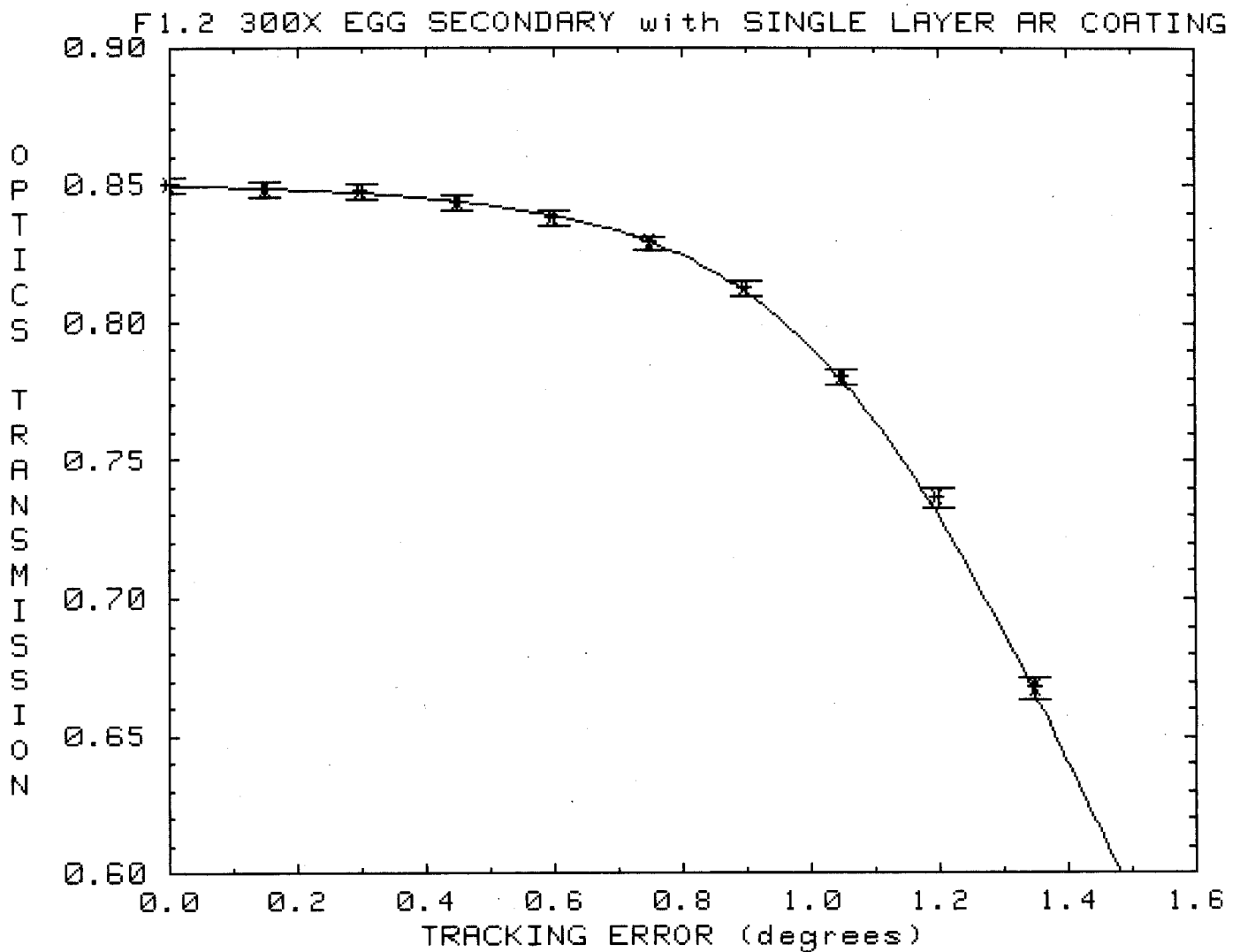


Figure 9: Optical transmission (short-circuit current weighted) of the complete optical system versus tracking error in the 300X egg-shaped secondary example with a single layer AR coating.

If no economically feasible AR coating can be developed, the secondary lens would need to be used without an AR coating. The transmission curve for that case is shown in Figure 10. This is the worst case transmission curve.

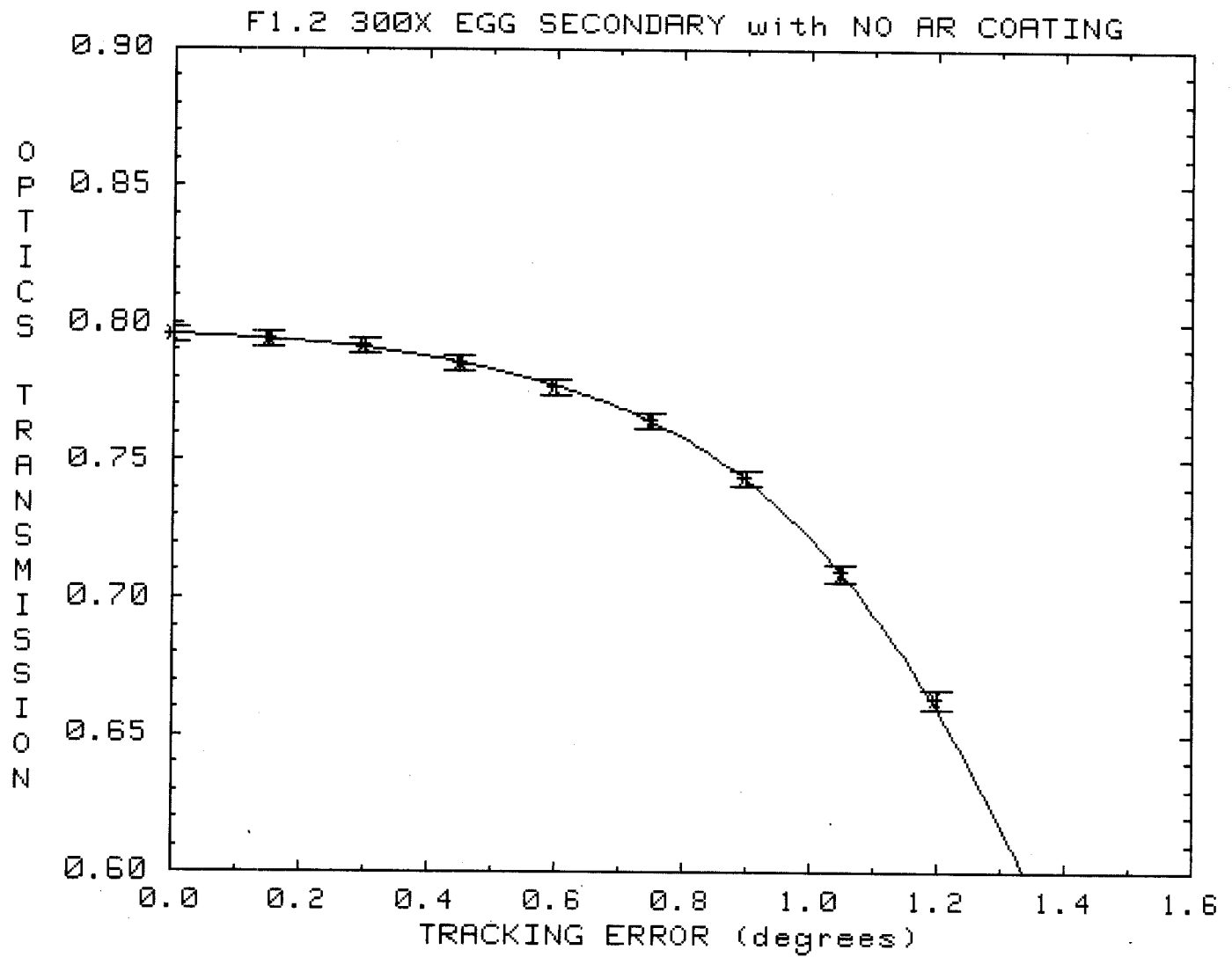


Figure 10: Optical transmission (short-circuit current weighted) of the complete optical system versus tracking error in the 300X egg-shaped secondary example with no AR coating.

As mentioned earlier, this double imaging set-up is not only more tolerant of tracking errors, it is also more tolerant of mounting errors. Figure 11 shows the optics transmission as a function of mounting error in the X-Y plane (parallel to the lens).

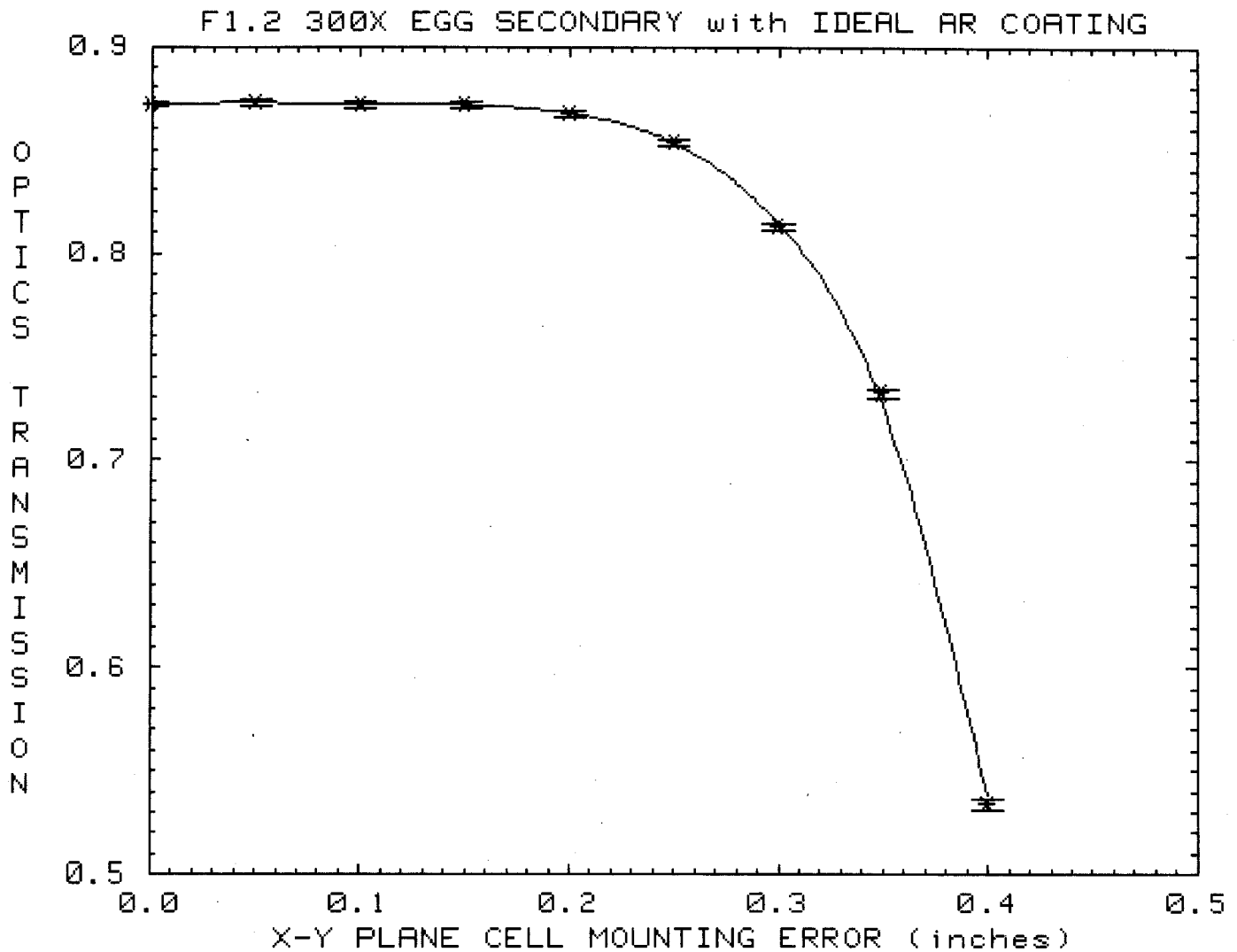


Figure 11: Optical transmission (short-circuit current weighted) of the complete optical system versus mounting error in the cell plane for the 300X egg-shaped secondary example.

Figure 12 shows that the tolerance of X-Y mounting errors extends to flux uniformity.

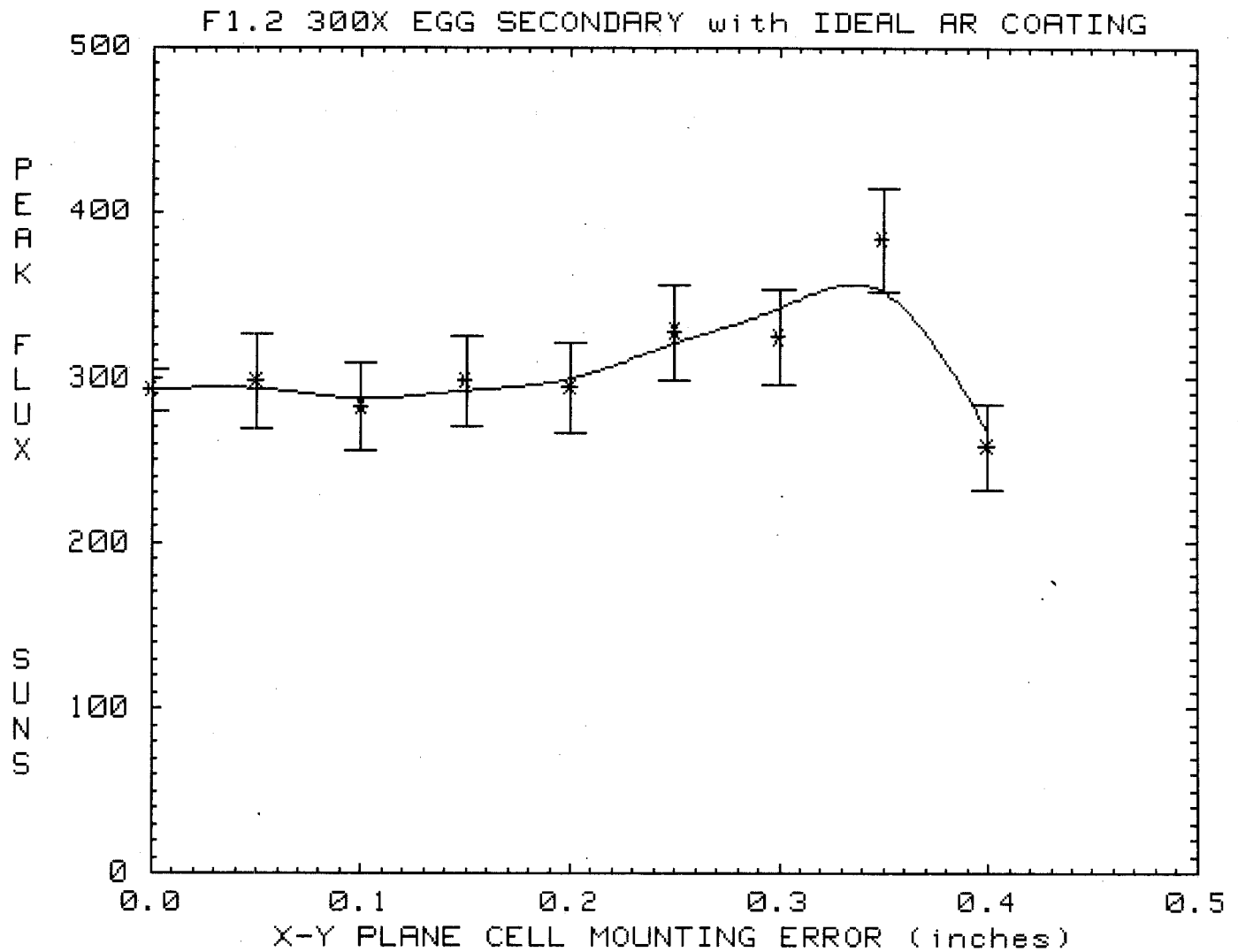


Figure 12: Peak flux density (short-circuit current weighted) of the complete optical system versus mounting error in the cell plane for the 300X egg-shaped secondary example.

Insensitivity of the optical transmission to the spacing between the Fresnel lens and the secondary-cell assembly is shown in Figure 13. This is the depth-of-field phenomenon referred to earlier.

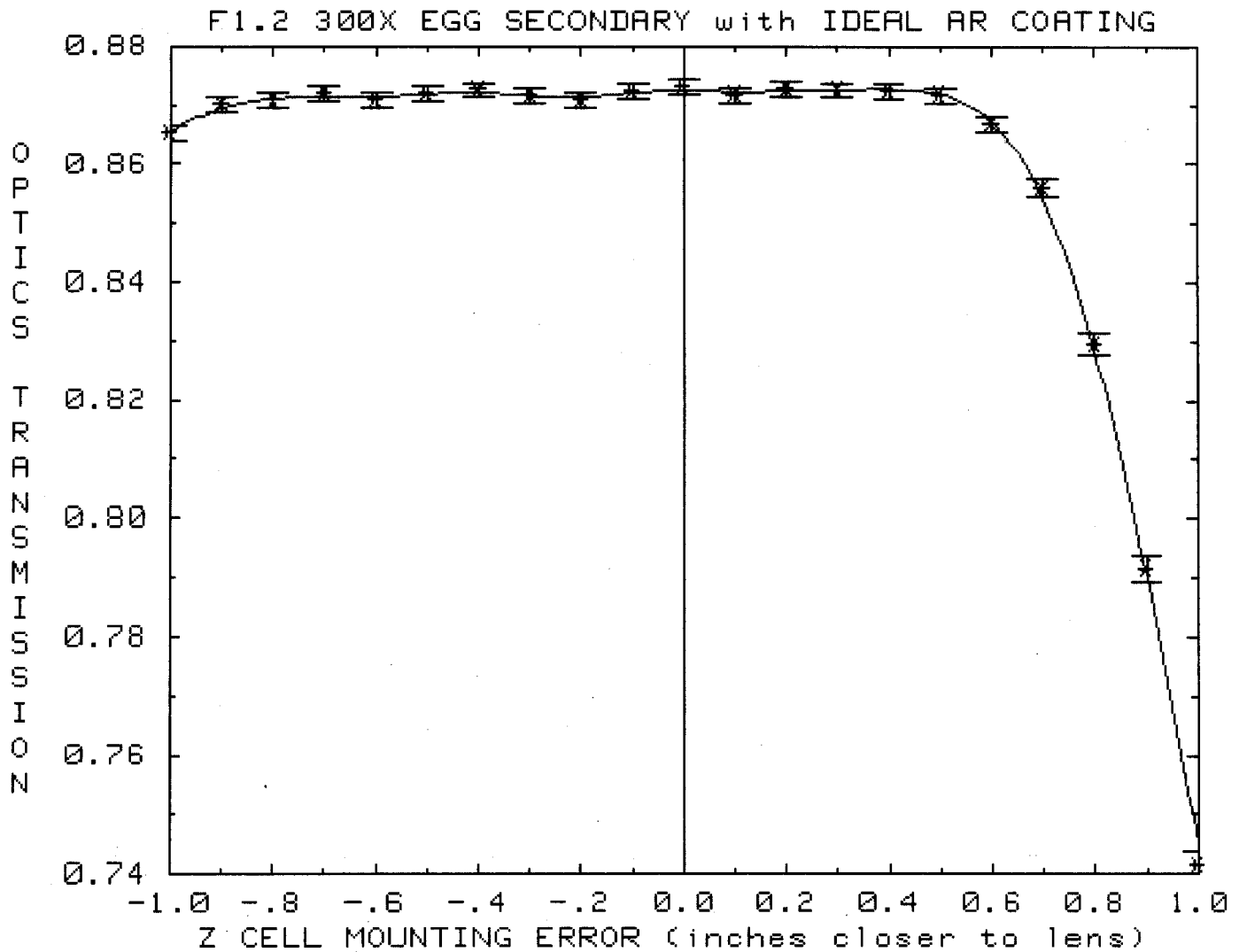


Figure 13: Optical transmission (short-circuit current weighted) of the complete optical system versus mounting error perpendicular to the cell plane for the 300X egg-shaped secondary example.

The peak flux as a function of the lens-to-cell assembly mounting error is shown in Figure 14. A reasonable specification for this parameter would seem to be ± 0.4 inches.

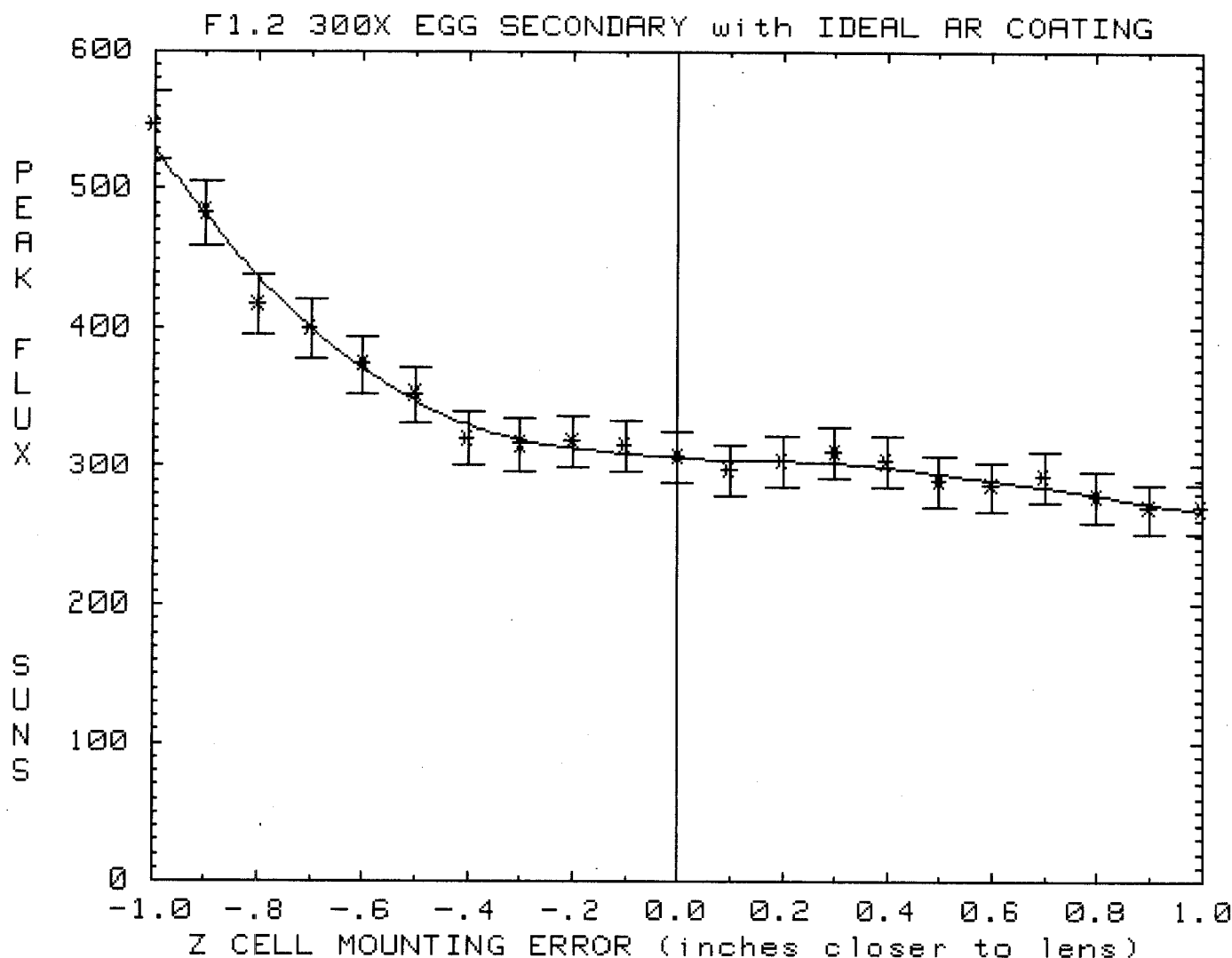


Figure 14: Peak flux density (short-circuit current weighted) of the complete optical system versus mounting error perpendicular to the cell plane for the 300X egg-shaped secondary example.

Consider the ramifications of these kinds of allowable tolerances. The normal error budget for current modules can be enlarged in almost every area. The larger error budget means thinner, lighter, lower cost materials could be used in the construction of a module. Lighter modules and the increased allowable pointing error would mean a lighter and cheaper frame to hold the modules. The cost savings could go on and on.

The Single Surface Imaging Secondary

The optical system discussed to this point has many advantages over the reflective cone systems currently used. It still has a few disadvantages though. The cell surface is unprotected, and the optical transmission is reduced by the reflection loss at the secondary exit optical surface. One further refinement will eliminate these two disadvantages. One normally thinks of a lens as having two surfaces with air on both sides, but that is not necessary. A single surface between two materials of differing refractive index can act as a lens. Thus the cell can be placed "inside" the glass of the secondary lens (from an optical point of view)², and the lens can still be made to function as described on the earlier pages. This would be physically implemented by building a lens that is half of an ellipsoid on the top, and shaped like a cylinder or a cone on the bottom. The bottom surface of the cylinder or cone would be flat and would be glued directly to the cell with a flexible optical cement that has roughly the same index of refraction as the glass. Figure 15 shows a side view of a system using the single active surface secondary, sometimes referred to as the SILO (SIngLe Optical surface) design.

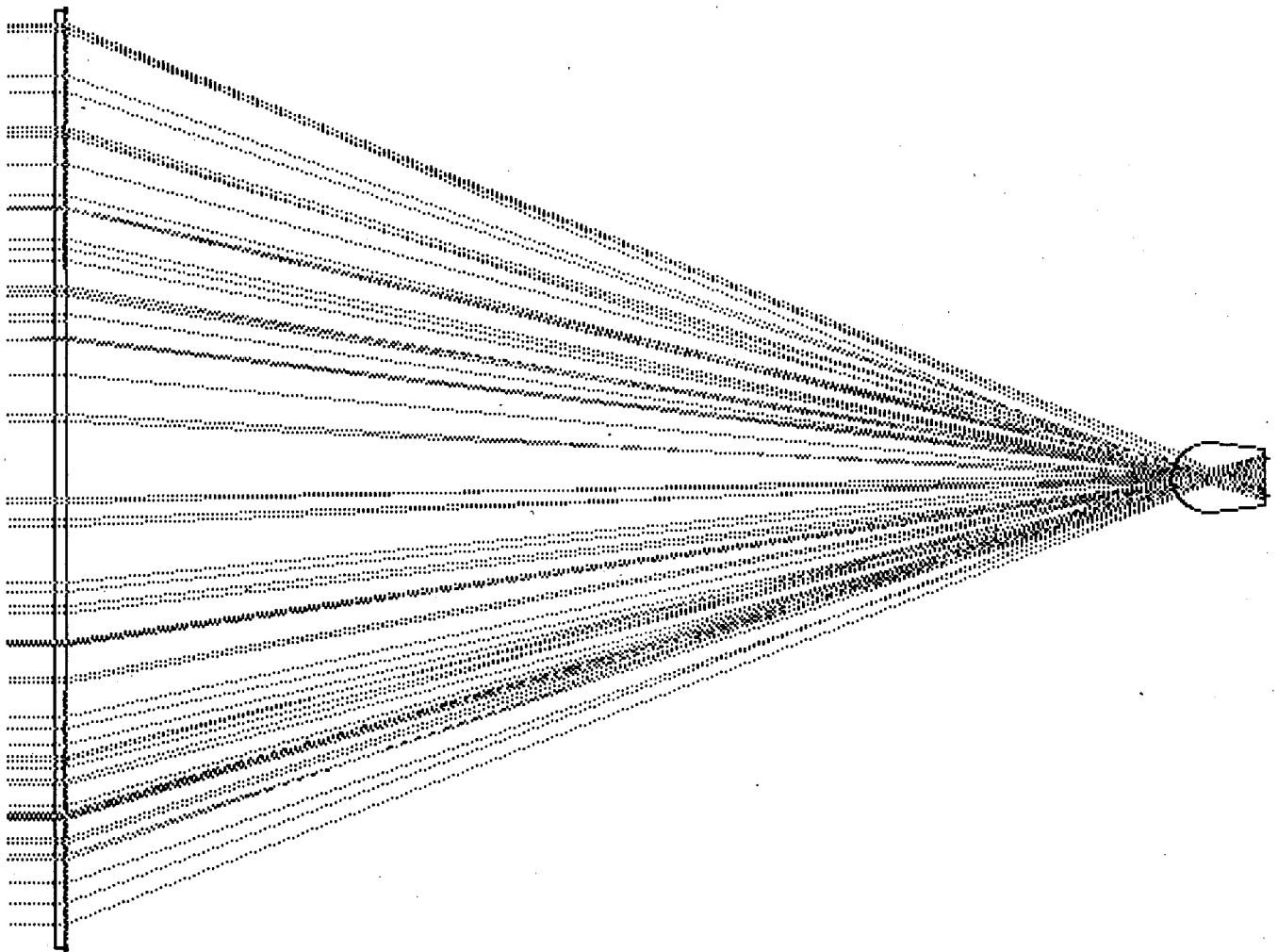


Figure 15: Example of a Single Surface Imaging Secondary Concentrator.

² Warren W. Smith, Modern Optical Engineering, The Design of Optical Systems (New York: McGraw-Hill Book Company, 1966), p. 233.

Some might argue that this system still has an extra optical reflection loss at the secondary lens input surface that is not there in a metal cone secondary system. In fact, the metal cone system may require a cell covering of some type to achieve acceptable cell lifetimes in the field. This cell covering could introduce a similar optical loss, in addition to the losses due to the imperfect reflectivity of the aluminum cone. Since all rays pass through the glass, the SILO lens will have a significant absorption loss unless a low absorptivity glass such as BK7 is used.

Figure 16 shows a close-up view of the secondary and the cell. The cell is shown along its diagonal. The two lines under the cell indicate the width of the cell along its side.

The secondary sides could be straight, but in fact in an actual part they would be slanted in toward the cell to make the piece moldable, as they are shown here. Only the top surface is optically active, so only the top surface needs an optical finish. The sides can be whatever shape is necessary for moldability and to clear other parts of the cell assembly. The flat bottom surface can be somewhat rough (optically) since it is filled in by the glue that glues the secondary to the cell. Appropriate glues have been examined by various Sandia contractors who used TIR secondaries on photovoltaic cells.

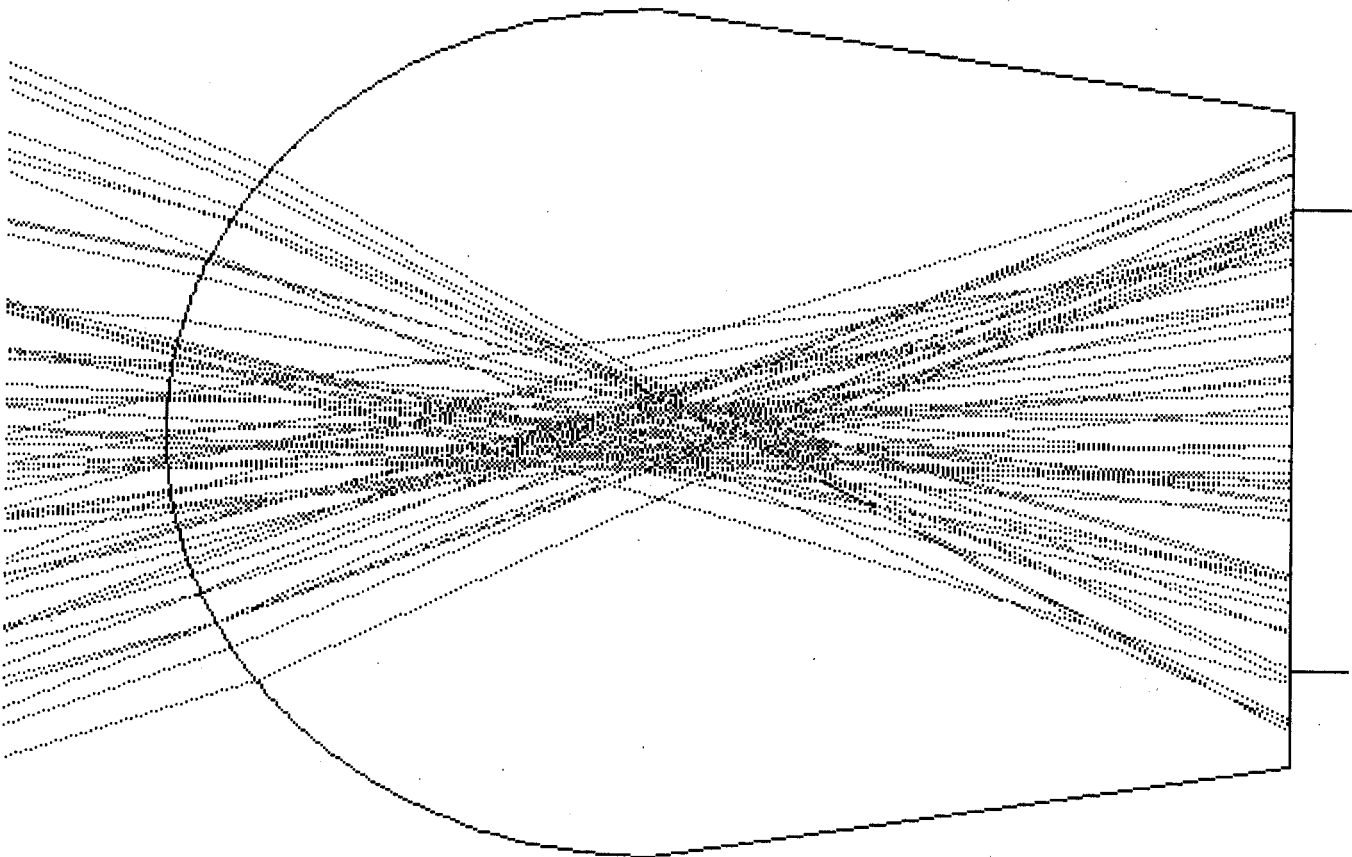


Figure 16: Close-up of the secondary lens and cell assembly in a SILO design.

This SILO secondary may look similar to a TIR secondary, especially when manufactured with slanted sides, but optically it is a completely different approach. The conical sides on a TIR secondary are optically active. TIR secondaries proved hard to mold and hard to mount, because of the tolerances required on the corner where the secondary met the cell. This SILO secondary has no such requirements. Hence the similarity in physical appearance should not cause those who have rejected TIR secondaries to reject this approach.

It is instructive to calculate the performance of a specific SILO design. For comparison purposes, we will look at the calculated performance of a 300X geometric concentrator module while keeping as many of the parameters as possible the same as in the earlier example using an egg-shaped secondary. The cell is square, the primary Fresnel lens is a 7-inch square compression-molded lens with 0.06-inch wide facets, and the lens-to-cell spacing is 12.518 inches. The secondary is molded out of BK7 glass. The secondary is composed of half of an ellipsoid on the top and a cylinder with slanted sides on the bottom. This particular secondary has for its top surface half of an ellipsoid with a minor axis of 0.740 inches and a major axis of 0.836 inches. The bottom part is a cylinder or a cone 0.740 inches in diameter at the top and 0.555 inches high (less the thickness of the glue). Thus the total height from the cell front surface to the top surface of the secondary ellipsoid is 0.978 inches. The bottom diameter of the SILO secondary would be equal to or greater than the cell diagonal.

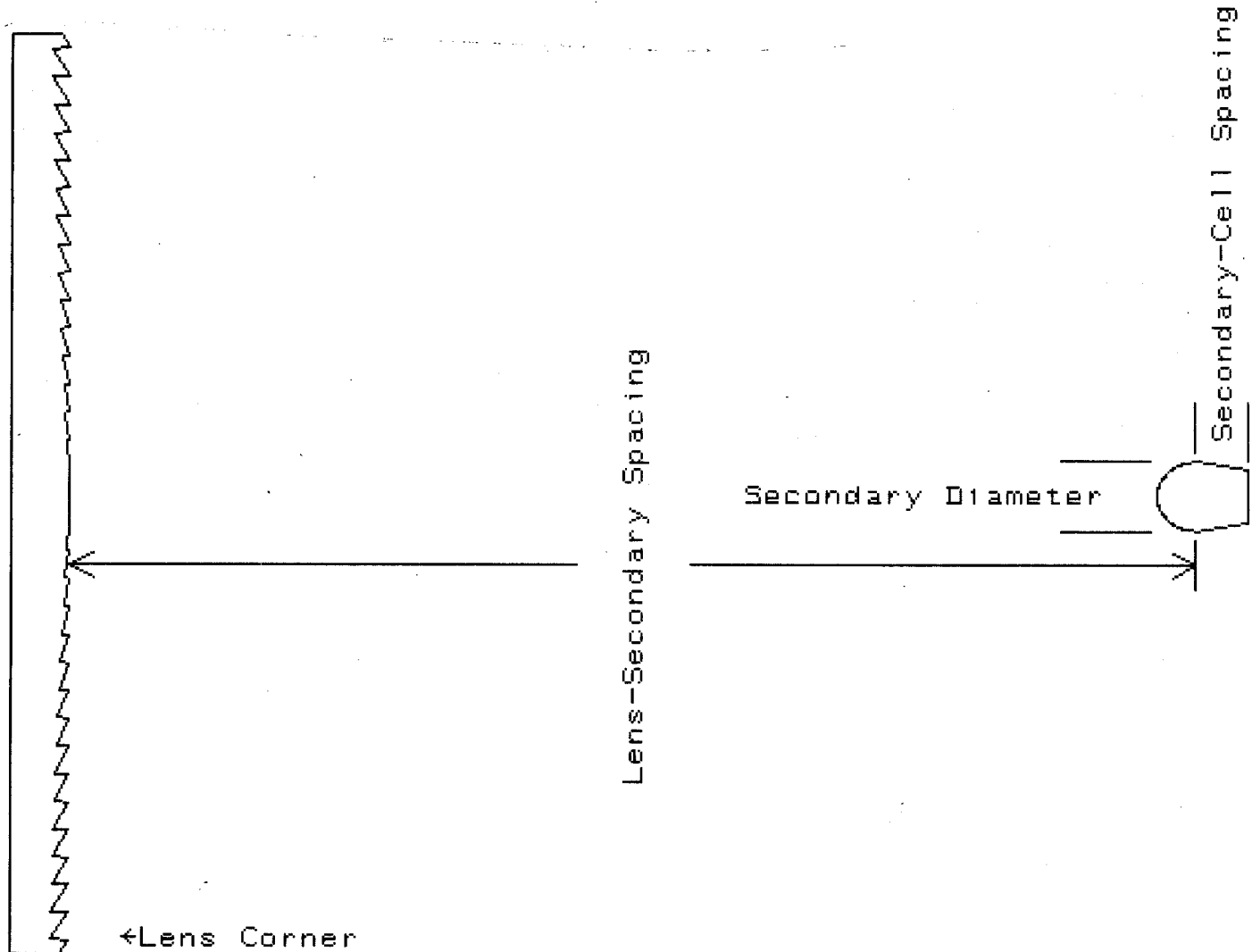


Figure 17: The SILO optical system used for modeling.

Figure 18 shows, in a side ray trace view, the imaging properties of the SILO design with light incident at three discrete points on the primary Fresnel lens (the center, the corner, and the center-to-edge distance). An important part of the design is that most rays that do not go through the imaging points miss in a direction toward the center of the cell, so they still land on the cell; they do not miss it. Another important point is that most rays hit the cell at close to perpendicular incidence, unlike the metal cone concentrator in which rays bouncing from the cone sides hit the cell at a glancing angle. This is an advantage, because the reflectivity losses of the cell increase substantially as the light incidence angle exceeds 40 degrees from the perpendicular for a flat-surface cell or 60 degrees from the perpendicular for a textured cell.

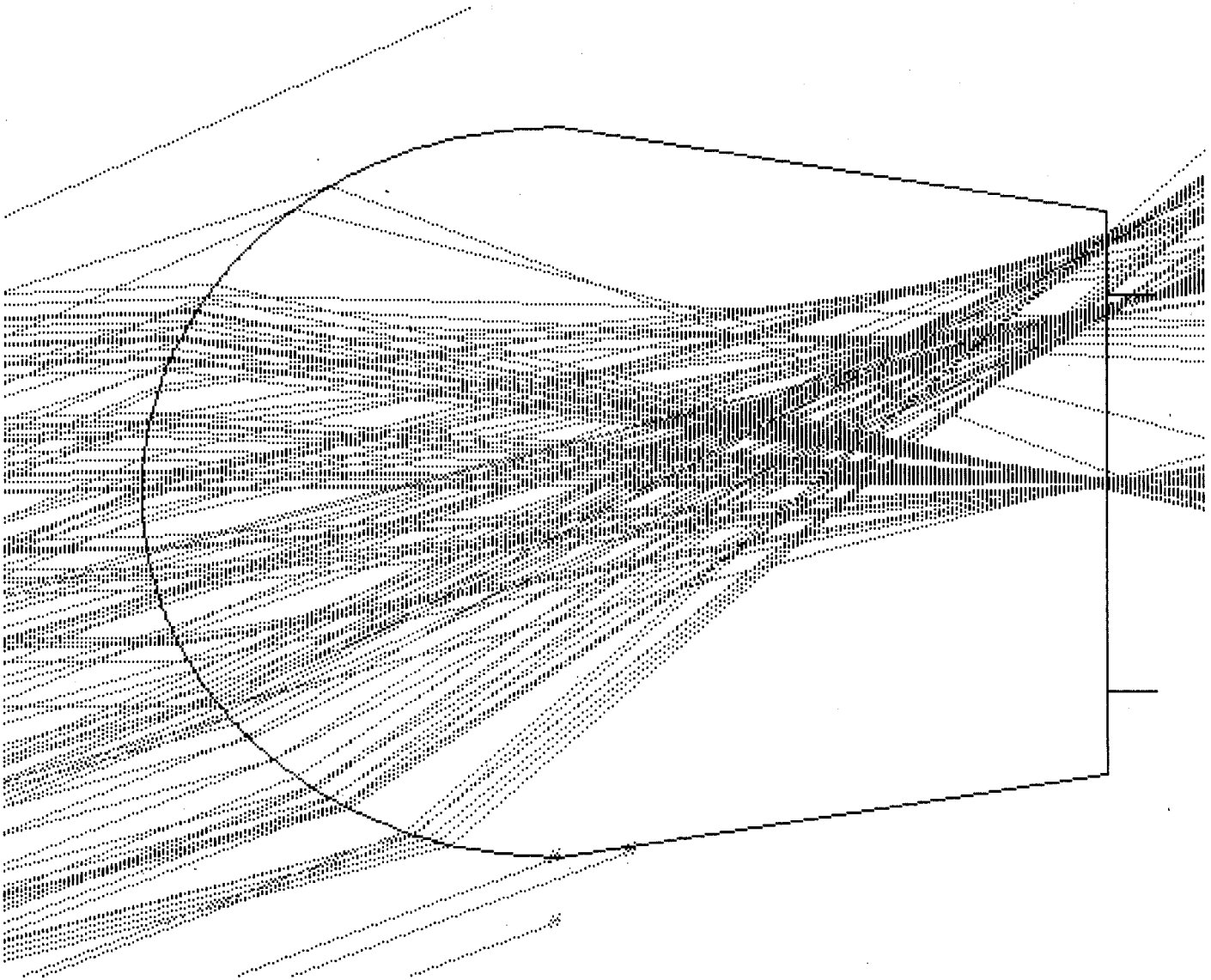


Figure 18: Close-up of a SILO cell assembly showing the imaging properties.

Figure 19 shows the spot diagrams for a rectangular array of fixed points on the primary lens. The imaging is, as before, not perfect, but it is certainly good enough. This diagram is roughly similar to Figure 4 for the egg-shaped secondary.

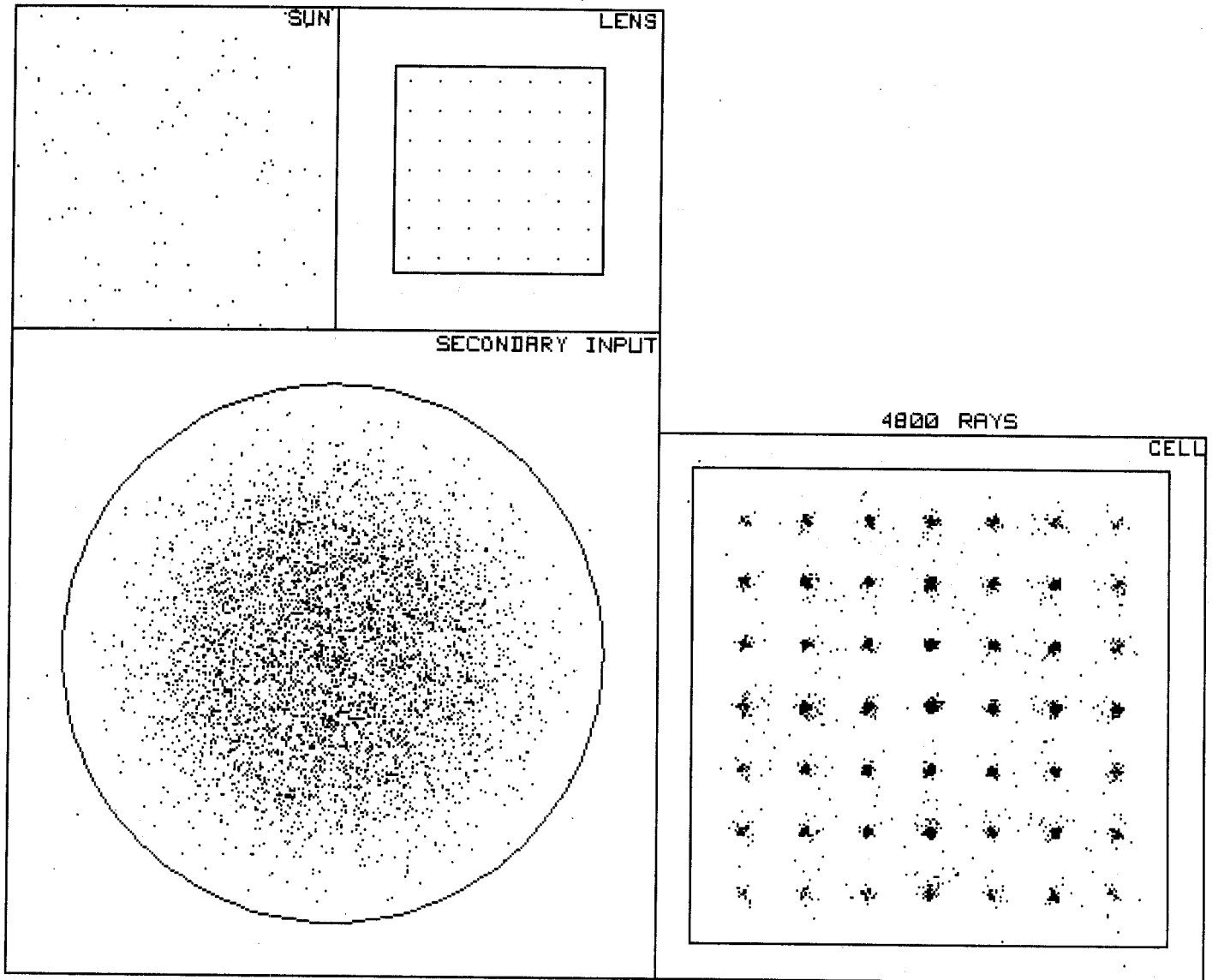


Figure 19: Spot diagram showing the imaging properties of the SILO secondary lens.

The computer printout, Figure 20, shows the ray spot patterns for this design with a normal sun and uniform illumination of the Fresnel lens when everything is in perfect alignment:

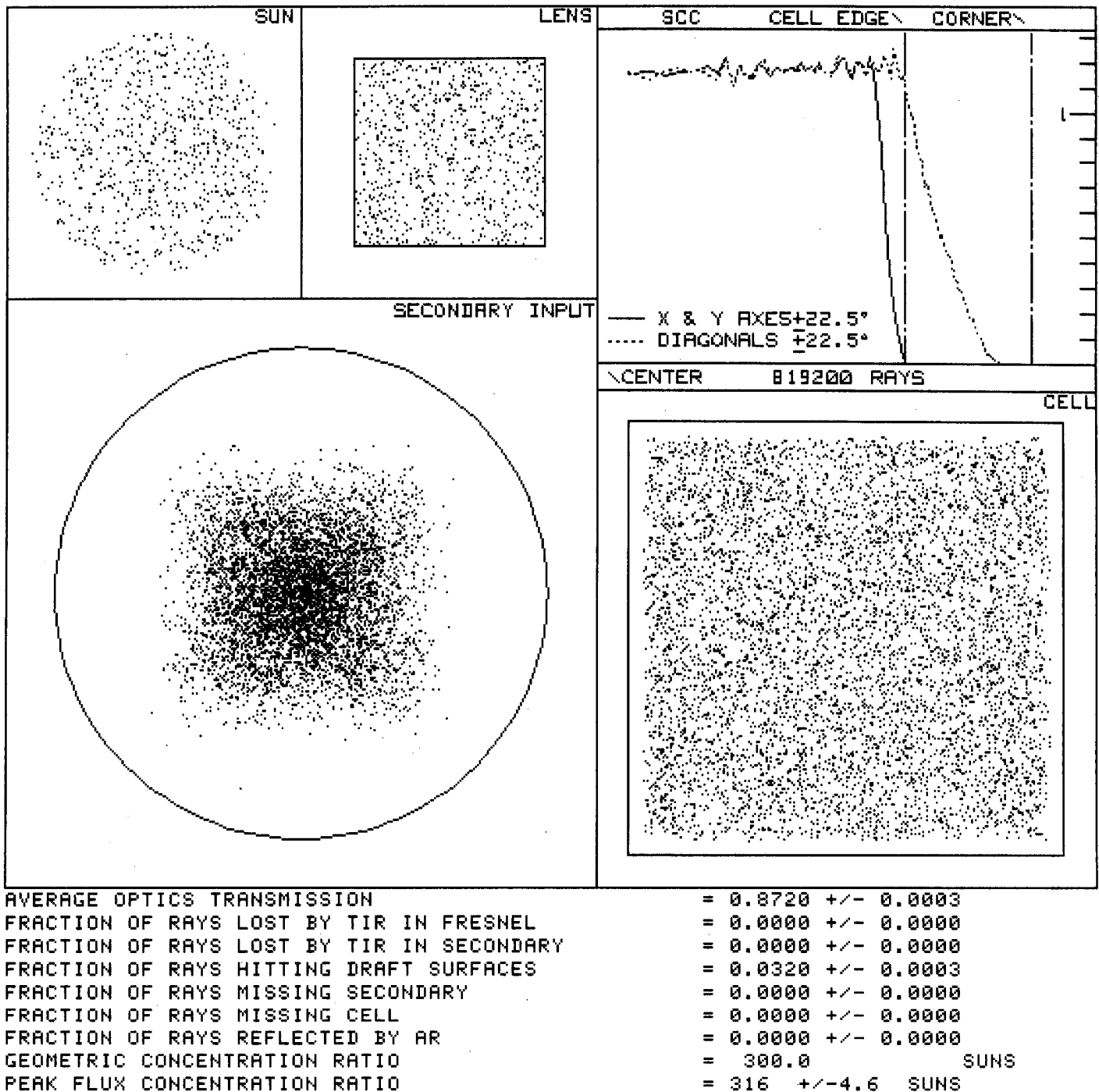


Figure 20: Monte Carlo ray trace spot patterns for the 300X SILO secondary example.

Figure 21 below shows the variation in short-circuit current flux over the area of the cell. The cell occupies all but the outer row of squares in the figure. Note that the flux is extremely uniform. The major difference between this figure and Figure 6 for the egg-shaped design is that this design has a slightly bigger guard band around the edge of the cell active area.

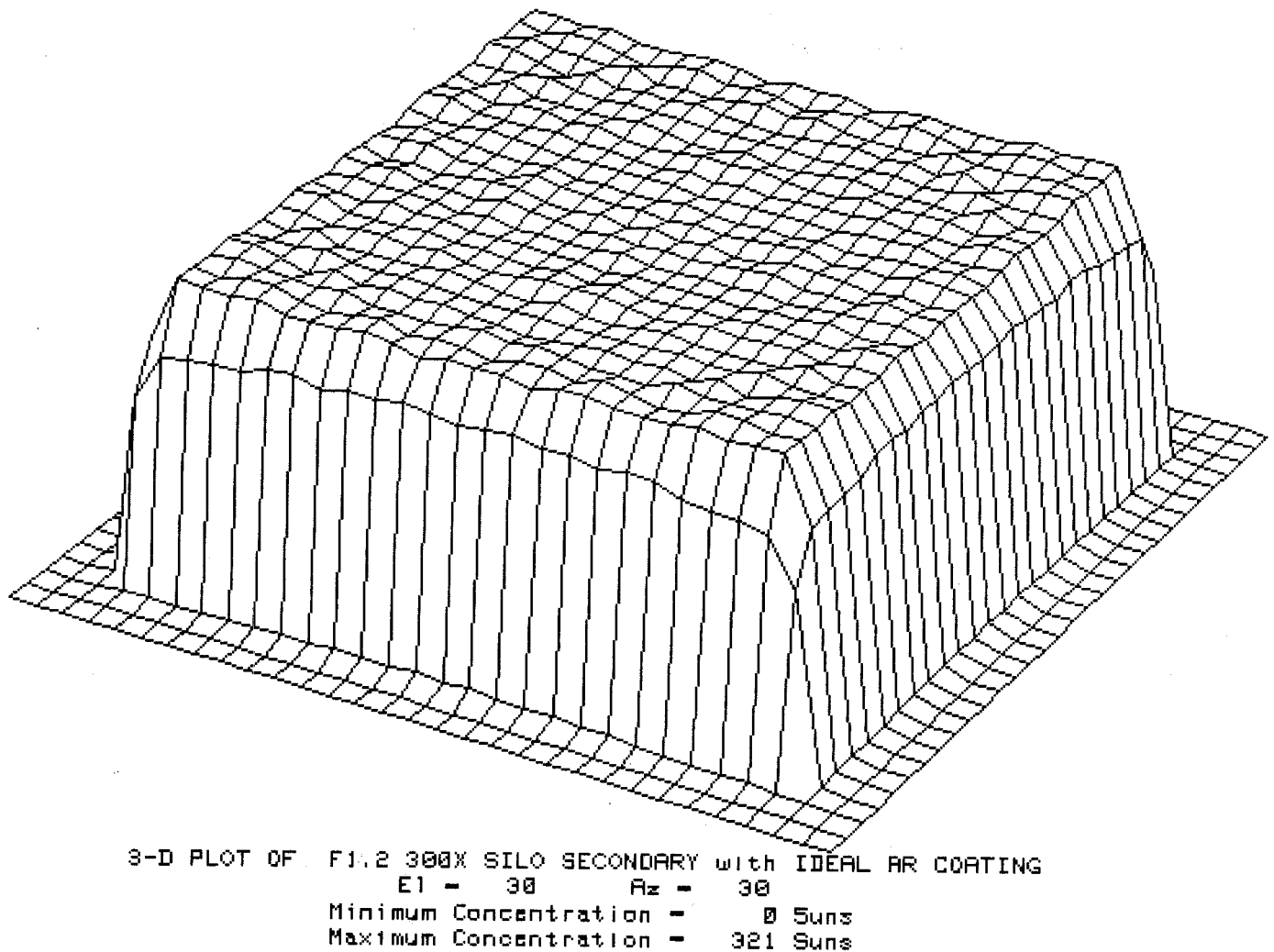


Figure 21: Short-circuit current flux for the cell in the 300X SILO secondary example.

The graph in Figure 22 shows the optics transmission versus tracking error with an ideal AR coating. It is virtually flat out to 0.7 degree, and quite usable out to a 1.1 degree tracking error. The f-number definition used here is the primary lens-to-secondary distance divided by the primary lens diagonal.

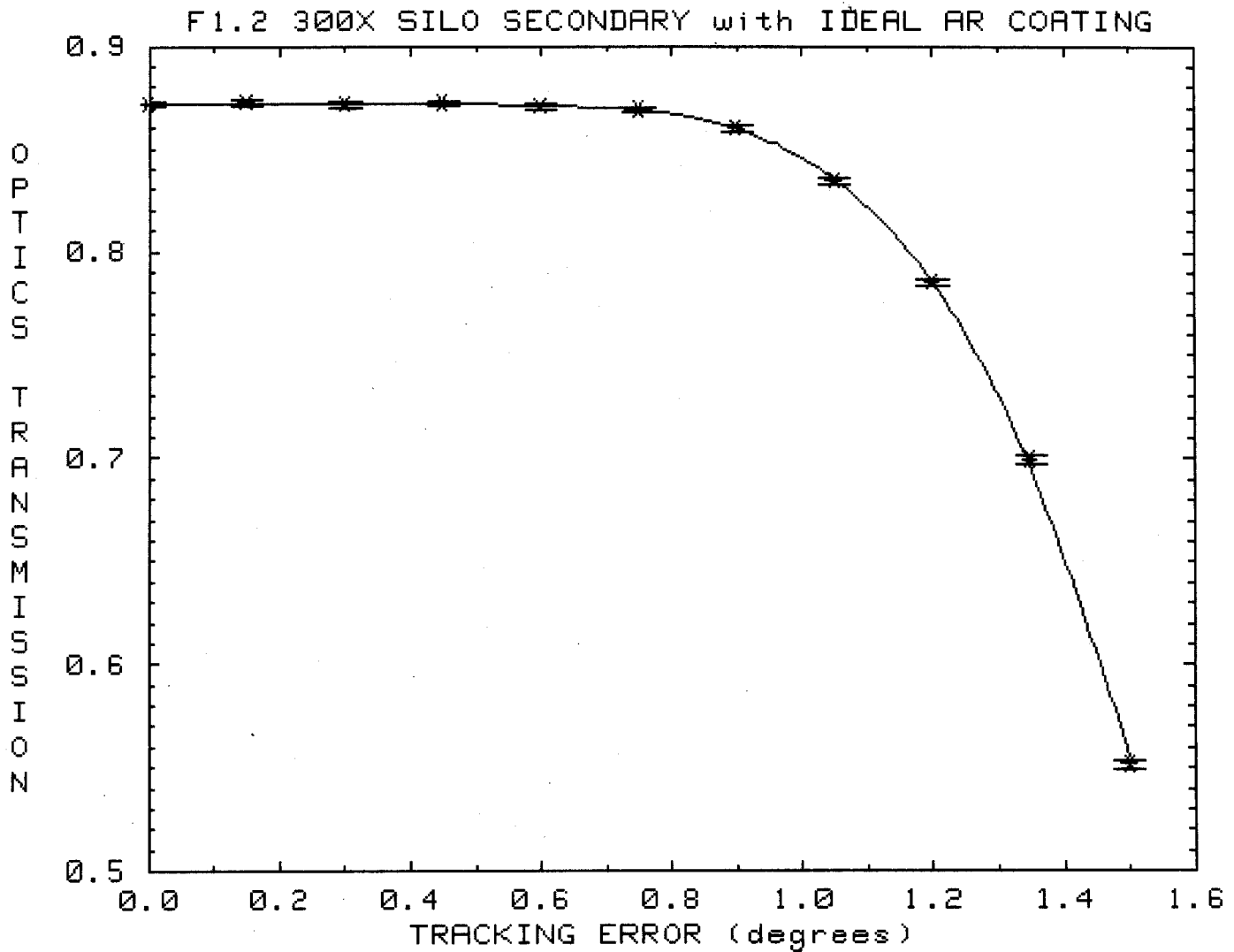


Figure 22: Optical transmission (short-circuit current weighted) of the complete optical system versus tracking error in the 300X SILO secondary example.

The peak flux occurring on the cell gives a good indication of how uniform the flux distribution stays. The curve in Figure 23 shows that the peak flux remains below 350 suns out to 0.8 degree tracking error, and only reaches 470 suns at a 1.35 degree tracking error.

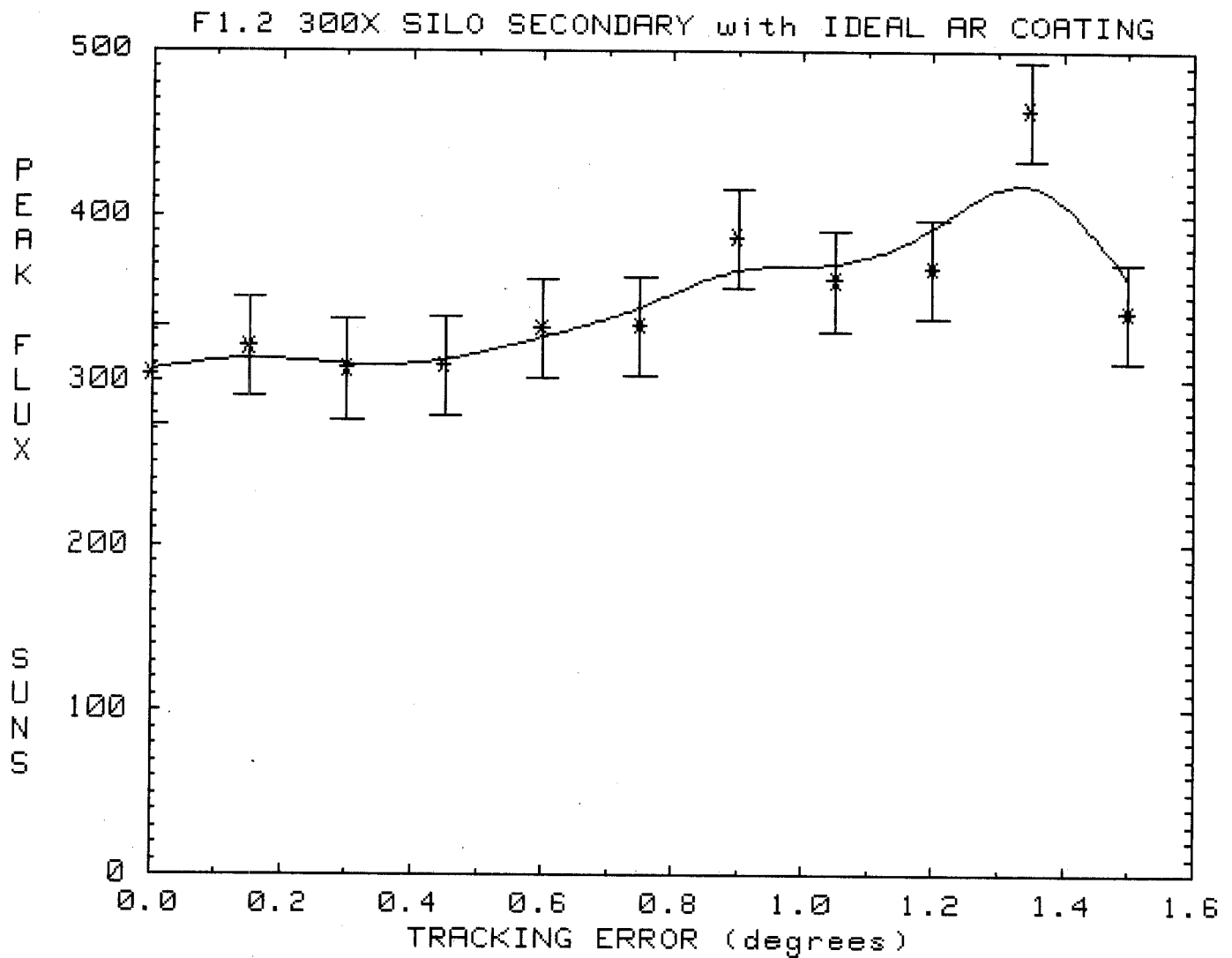


Figure 23: Peak flux density (short-circuit current weighted) of the complete optical system versus tracking error in the 300X SILO secondary example.

As with the egg-shaped secondary lens, the curves shown so far have been for an ideal multi-layer AR coating applied to the secondary lens. The same curves were calculated for a single layer AR coating of a material such as MgF. Such a single-layer AR coating may be economically viable. The transmission curve for that case is shown in Figure 24.

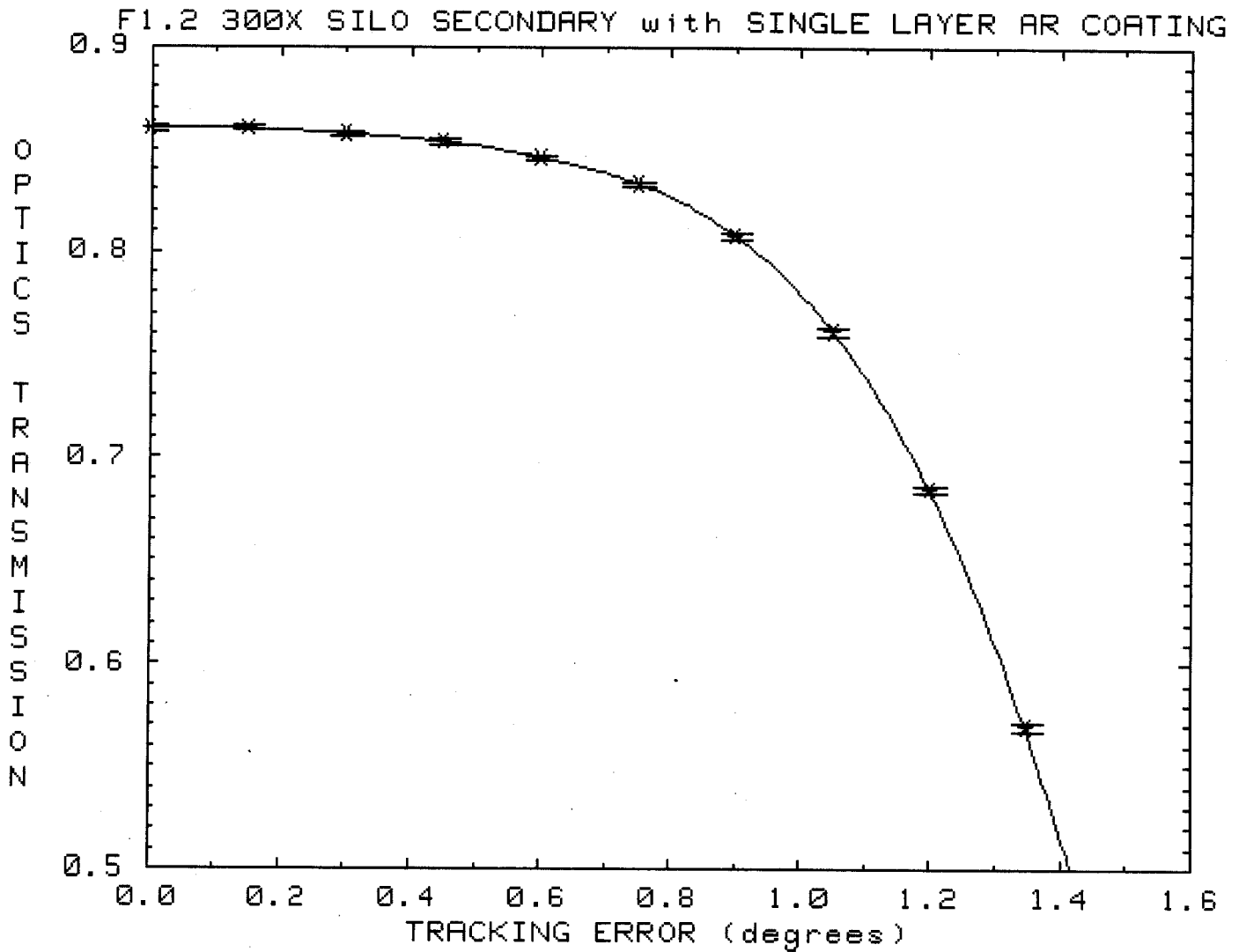


Figure 24: Optical transmission (short-circuit current weighted) of the complete optical system versus tracking error for the 300X SILO secondary example with a single layer AR coating.

The peak solar flux curve for a single layer AR coating on the secondary lens is shown in Figure 25.

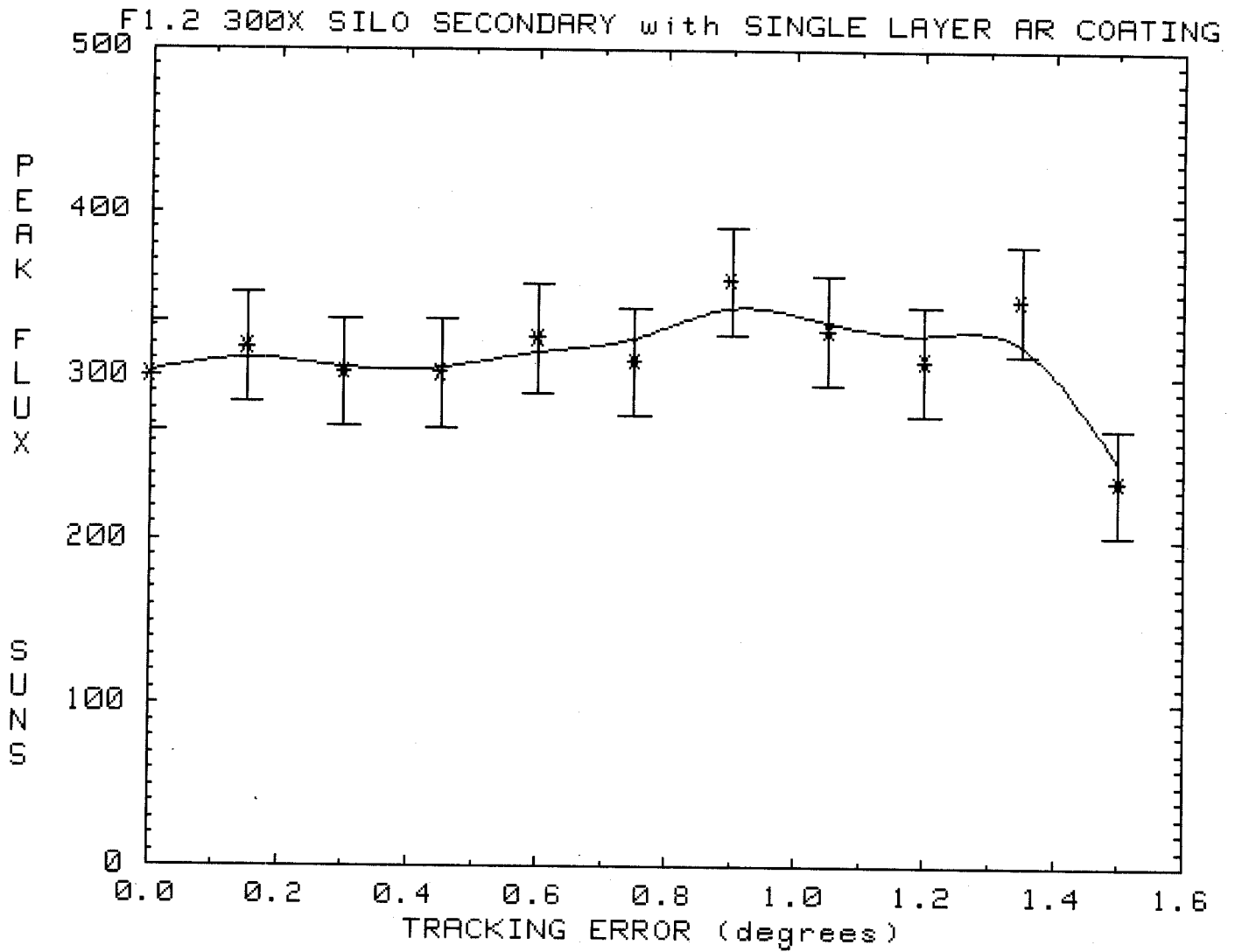


Figure 25: Peak solar flux (short-circuit current weighted) of the complete optical system versus tracking error for the 300X SILO secondary example with a single-layer AR coating.

If no economically feasible AR coating can be developed, the SILO secondary lens would need to be used without an AR coating. The transmission curve for that case is shown in Figure 26. This is the worst case transmission curve.

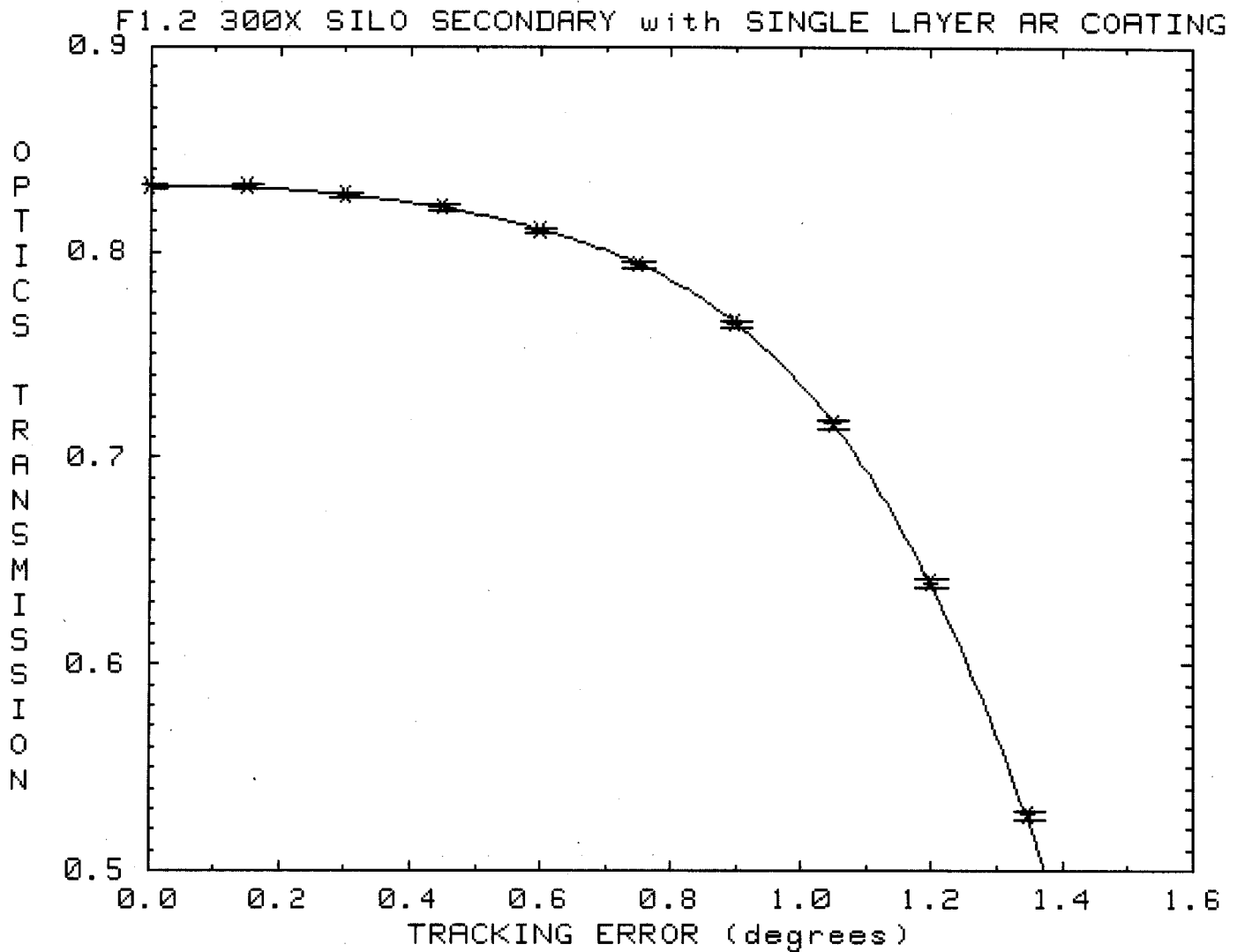


Figure 26: Optical transmission (short-circuit current weighted) of the complete optical system versus tracking error in the 300X SILO secondary example with no AR coating.

The peak solar flux curve for a SILO secondary lens with no AR coating is shown in Figure 27.

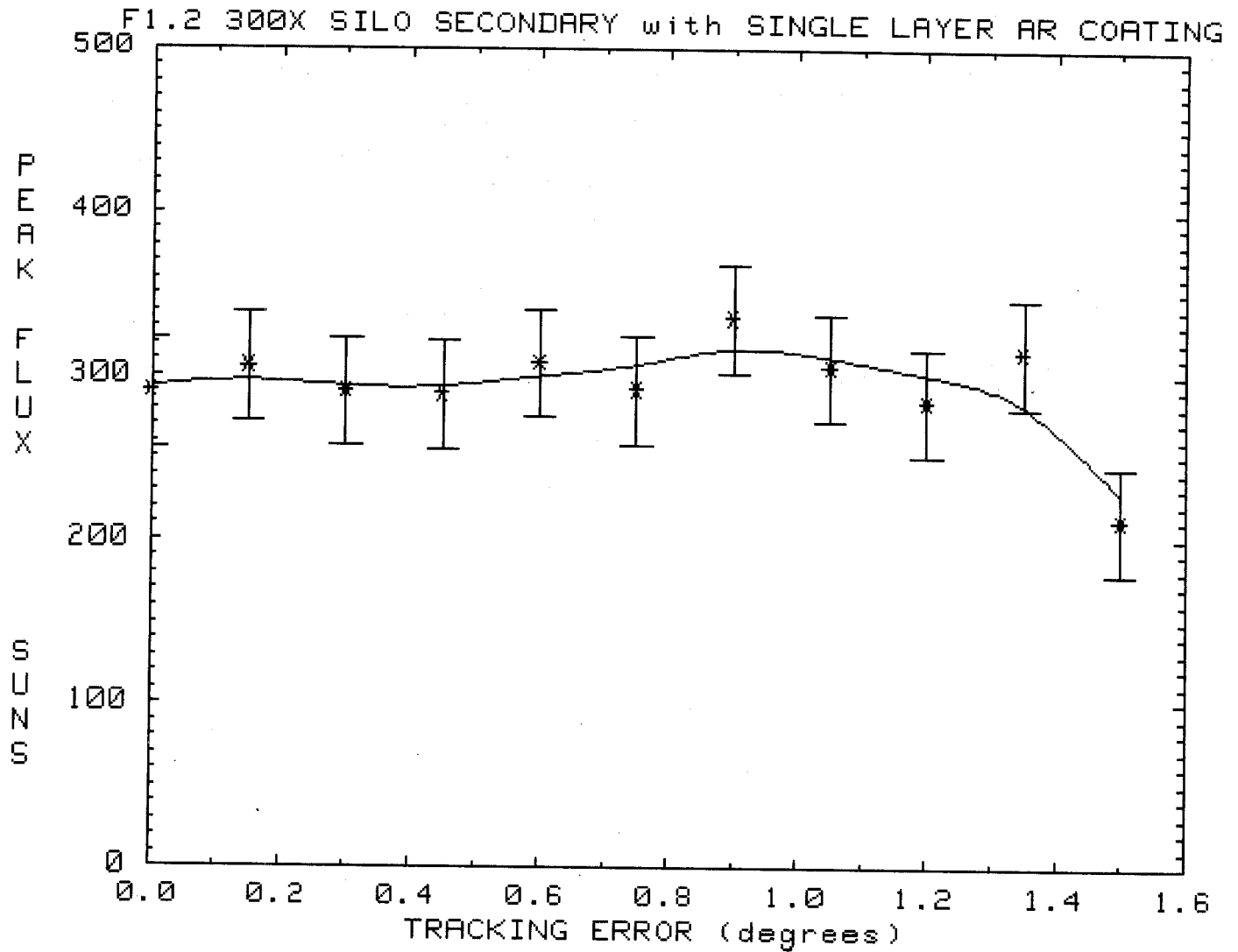


Figure 27: Peak solar flux (short-circuit current weighted) of the complete optical system versus tracking error in the 300X SILO secondary example with no AR coating.

The SILO secondary has a higher optical transmission (except in the case of ideal AR coatings) than the egg-shaped secondary. It also provides cell encapsulation, whereas the egg-shaped secondary does not. Is there, therefore, any disadvantage to choosing the single-surface secondary? There is one disadvantage. The egg-shaped secondary has a diameter of 0.890 inches, whereas the single active surface secondary has a diameter of only 0.740 inches. This is because the necessary optical power is split between two surfaces with the egg-shaped secondary, but all of the optical power must come from one surface in the SILO design. This smaller secondary cross-sectional area causes the curves of transmission versus any of the mounting or pointing errors to fall off slightly sooner, for example at 1.1° instead of 1.2° in the case of tracking error on the 300X system. If no AR coating is economically feasible, the advantages of the single active-surface secondary outweigh this minor disadvantage, and it is the design of choice for most applications. If an economic multi-layer AR coating can be found (unlikely), then the egg-shaped secondary is the best choice. If an economic single-layer AR coating can be found, then a detailed economic analysis would be necessary to see which is the better choice. Figure 28 shows the comparison for a 500X system.

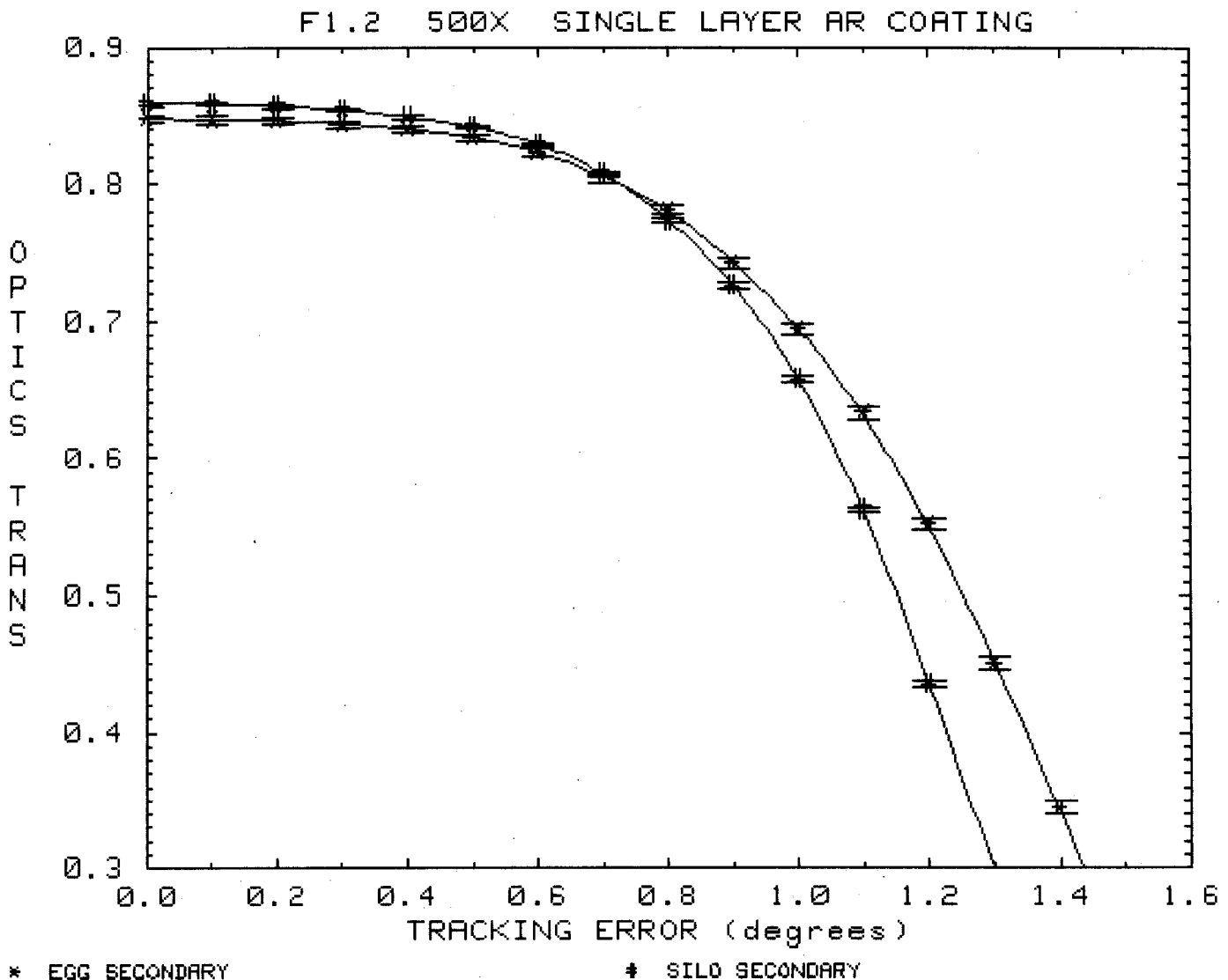


Figure 28: Comparison of an egg-shaped secondary with a SILO secondary.

System Design Considerations

In designing a system using a SILO secondary, we would like to know the optimum f-number of the primary lens and the maximum achievable concentration. To this end, a number of computer runs were done on a whole series of individually designed modules covering geometric concentration ratios from 100X to 10000X, and f-number's from 0.7 to 2.0. From the output of these computer runs, we can draw parametric curves that can be used in system design calculations.

In each case (each point on a curve) to be shown on the next several pages, a separate single-layer AR coating was assumed, and the Fresnel lens facet angles and the secondary lens design were optimized for that case.

Figure 29 shows the transmission of an entire 600X optics system (primary Fresnel lens + a BK7 secondary SILO lens) as a function of the primary lens f-number for different tracking errors. F-number is defined as the focal length (primary lens to secondary lens spacing) divided by the lens diagonal.

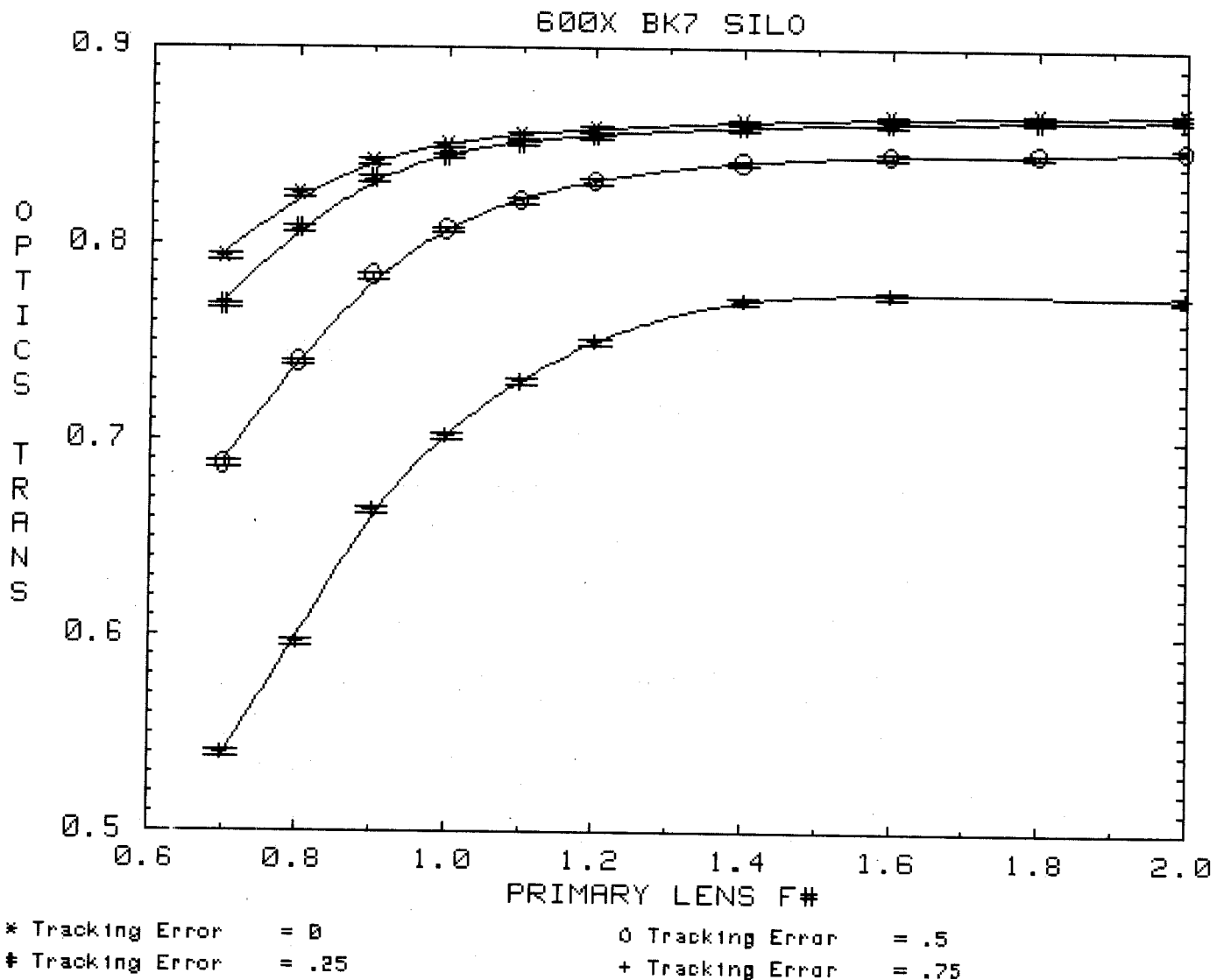


Figure 29: Transmission of a 600X SILO system versus primary lens f-number.

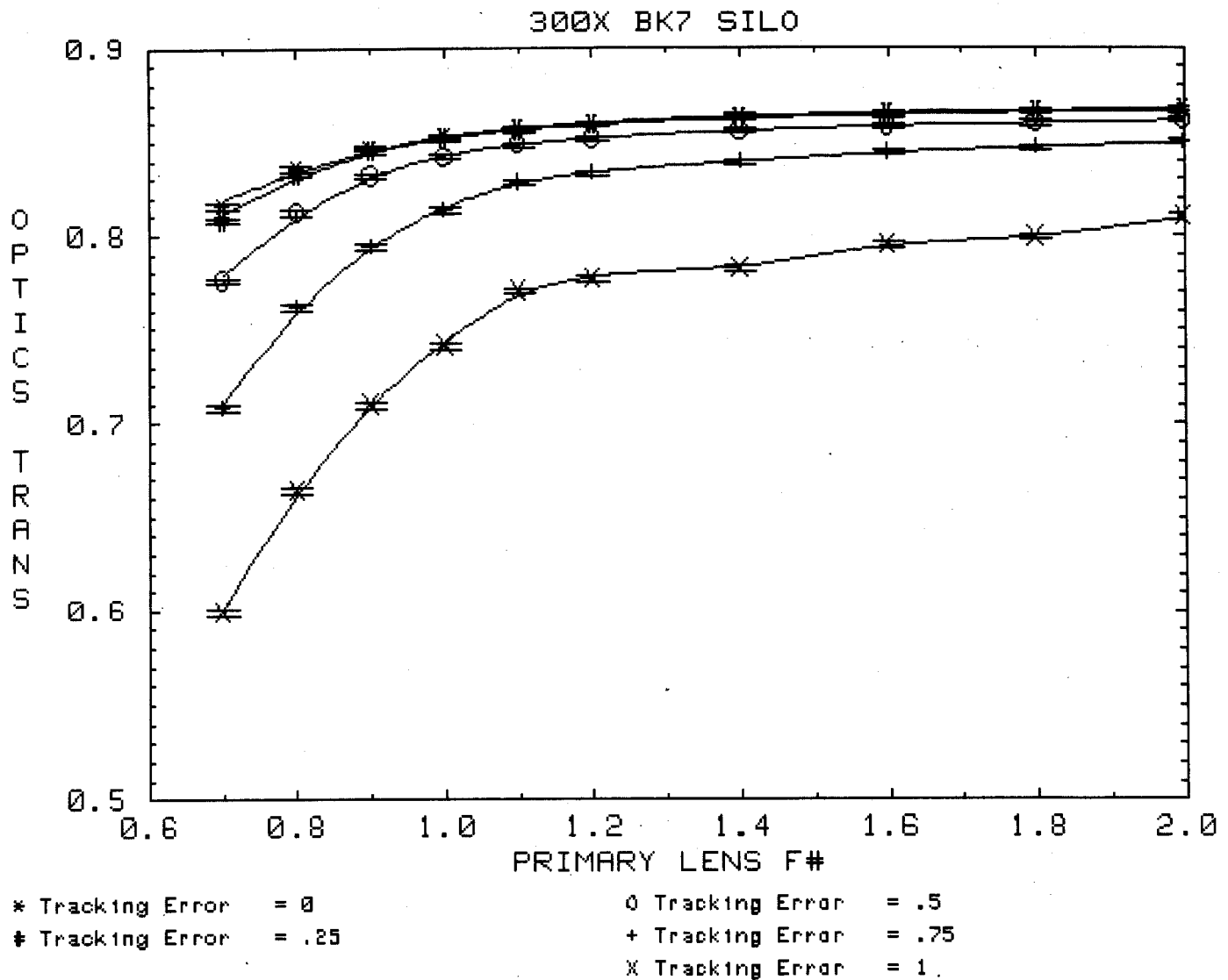


Figure 30: Transmission of a 300X SILO system versus primary lens f-number.

Figure 30 shows the same information for a 300X system. Note that below about $f-1.2$, the transmission fall off becomes sharper. Above $f-1.2$, they asymptotically approach a limit. As the f-number of the primary lens becomes larger, the image of the sun at its focal point enlarges, but the secondary lens also has a longer focal length, so it becomes larger. If the lenses had no aberrations, these two effects would exactly cancel, and all of these curves would be straight horizontal lines. Because the Fresnel lens aberrations worsen as the f-number becomes smaller, the curves in the figure drop. As f-number increase, the module becomes deeper and the size of the glass secondary increases, both increasing costs. An optimum f-number may be determined by balancing these curves against cost curves.

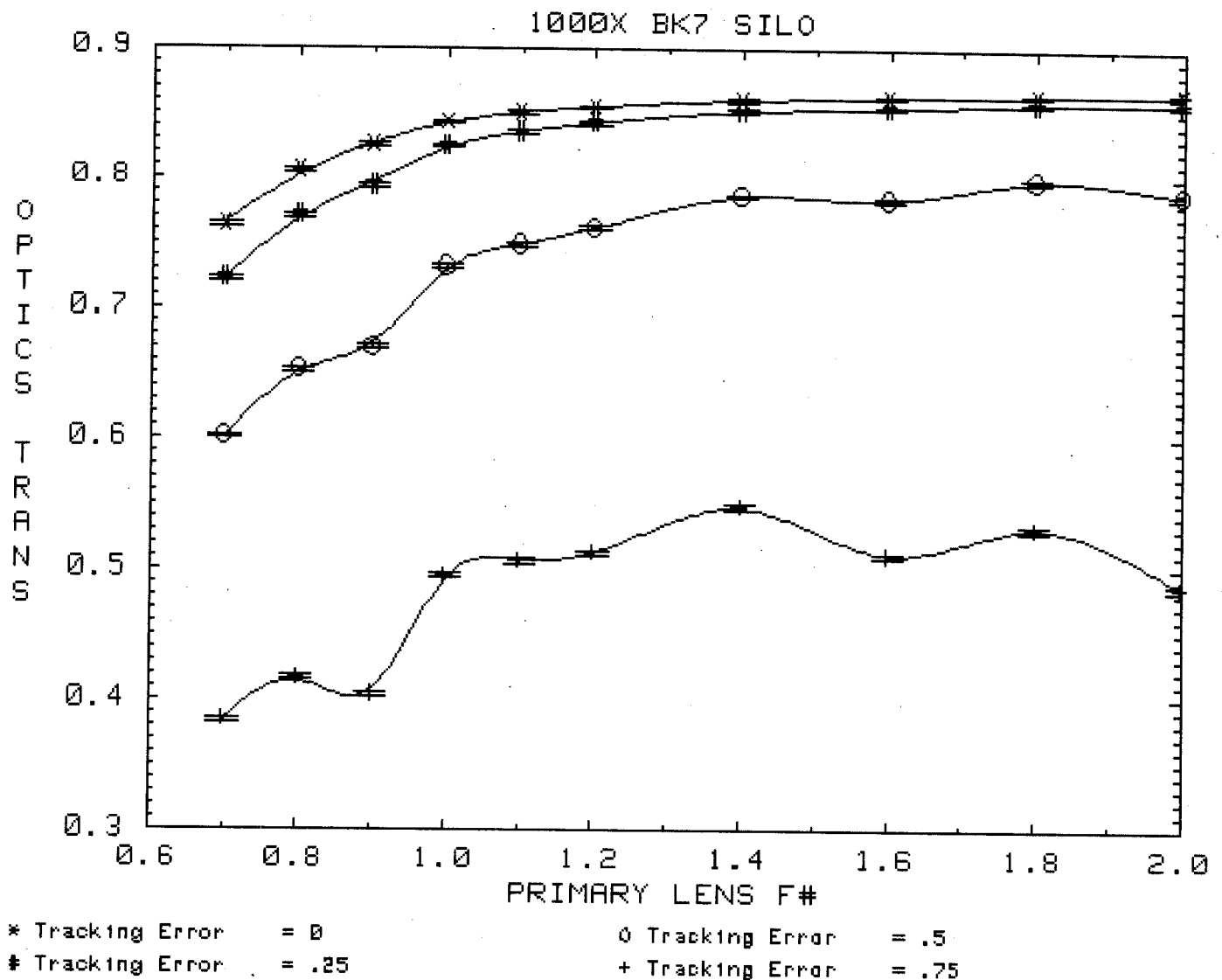


Figure 31: Transmission of a 1000X SILO system versus primary lens f-number.

Figure 31 shows the same curves, but for a 1000X system. As expected, the transmission numbers fall off more sharply with tracking error. Otherwise, the curves are basically similar to the curves on the previous two pages. (The additional "noise" in the curves is caused by the fact that each point involves a separate design. The designs were done by visually focusing the rays using the close-up side view of the ray traces in the James Associates computer code. This noise implies that if a real 1000X system is built, the focusing will have to be very carefully designed.)

This final figure, Figure 32, in the series shows the curves for a 3000X system for comparison. Note that the wider range covered by the vertical axis gives the appearance that the fall off at small f-number's is not as great, whereas in fact it is greater than the previous curves. This high a concentration is clearly not practical in a system with real tolerances.

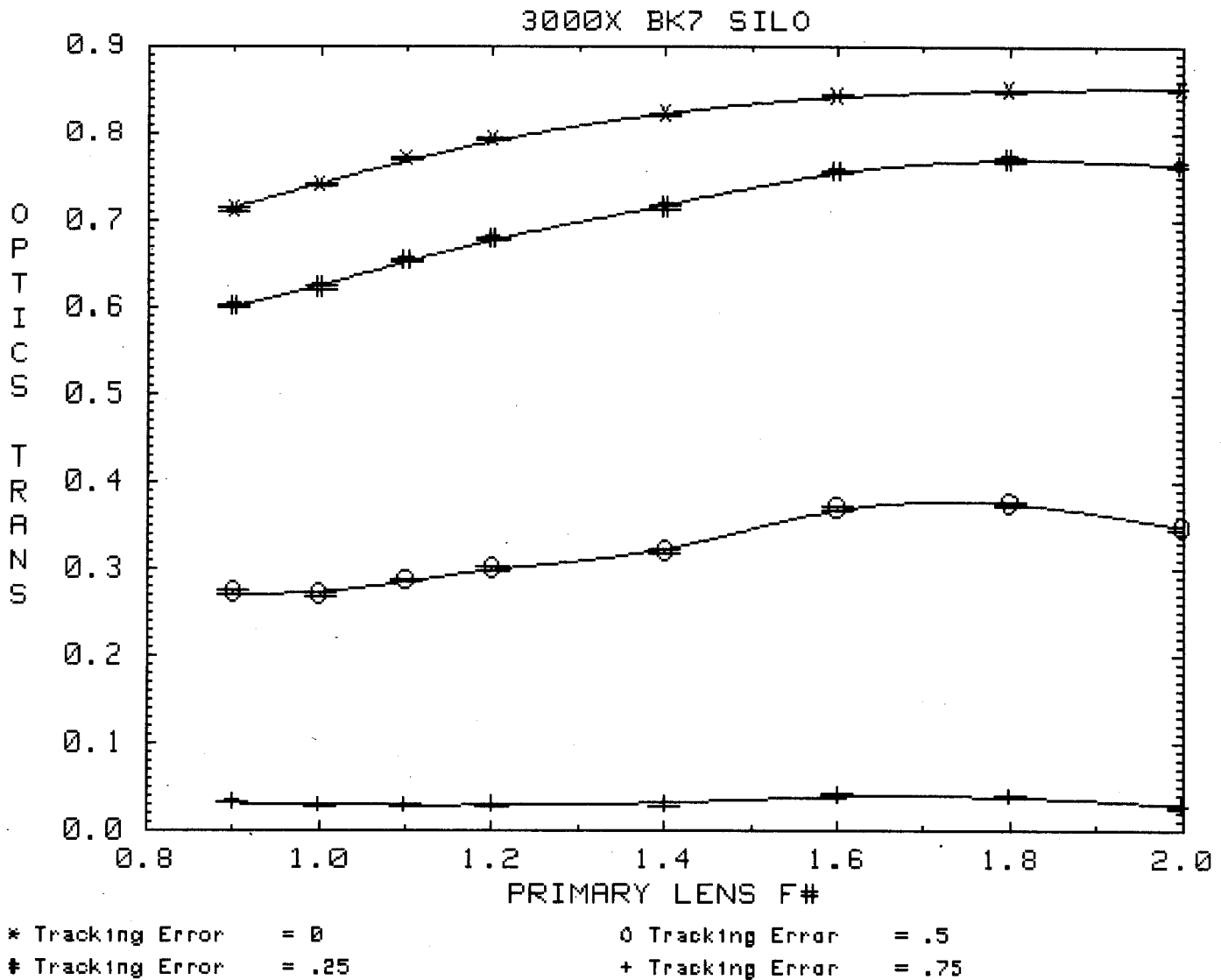


Figure 32: Transmission of a 3000X SILO system versus primary lens f-number.

Another way to look at these data is to examine the maximum geometric concentration ratio that can be used for different f-number's and different desired allowable tracking errors. This curve (Figure 33) was plotted assuming a requirement for an optical transmission $\geq .83$ with a single-layer AR coating on the secondary BK7 SILO lens.

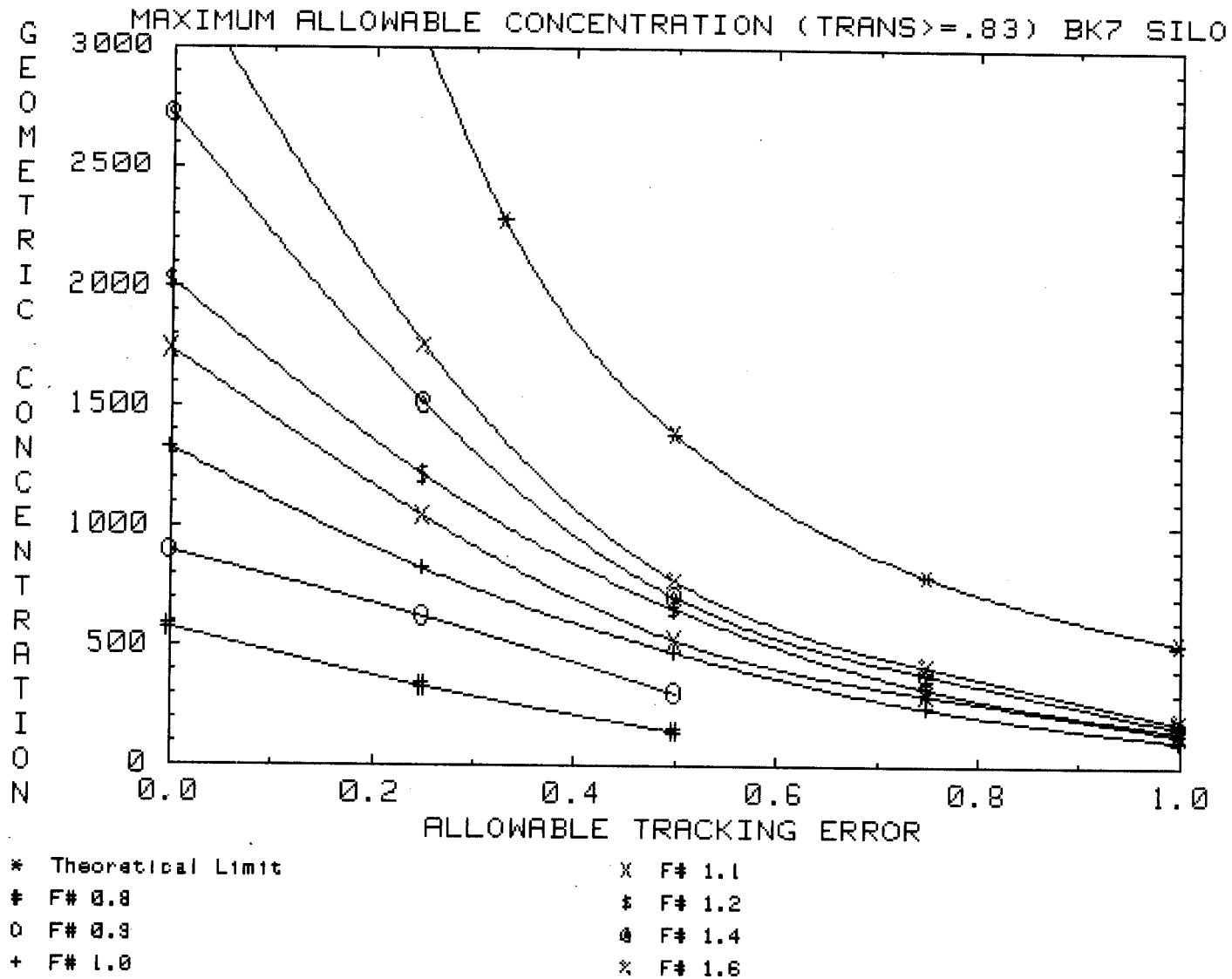


Figure 33: Obtainable geometric concentrations versus allowable tracking error and primary lens f-number.

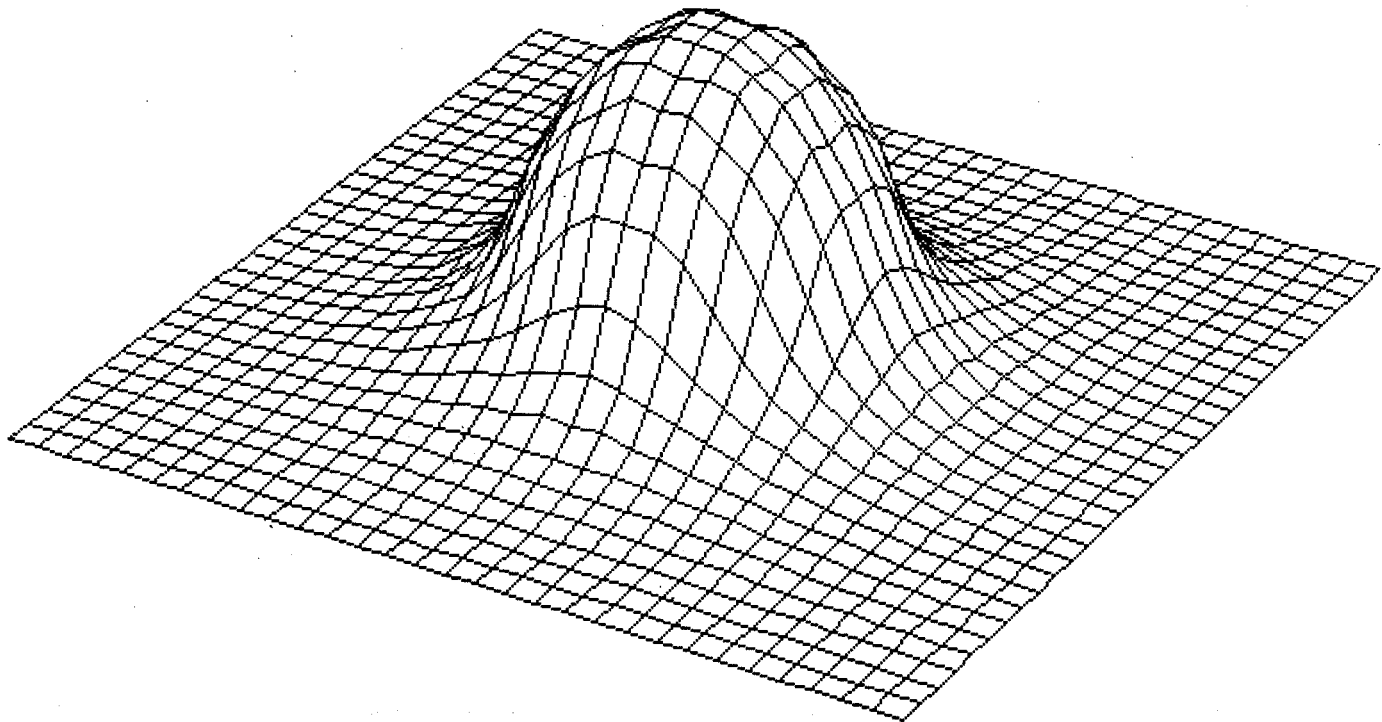
Clearly for cases with a very high cell cost, pushing the designer to high concentration ratios, a large f-number primary lens is preferred. For moderate concentration ratios, good transmission values can be obtained over a wide range of f-number's, but increasing the f-number increases the allowable tracking error. These curves can be used with curves of cost versus module depth and cost versus array stiffness to determine an optimum system design.

Properties of Glass Appropriate for an Imaging Secondary

Not all glasses are appropriate for use in this type of secondary optical element. There are four important properties to consider:

1. Moldability
2. Ability to withstand high solar flux levels
3. Refractive index
4. Optical transmission

The moldability criterion suggests using a plastic material, but plastics may be incapable of meeting the second criterion. Figure 34 shows the flux density that occurs in the middle of a 300X SILO secondary. It may well be that this 10000 sun flux would destroy a plastic lens, although it would be very nice if this were proven wrong.



3-D PLOT OF INTERIOR OF 300X SILO SECONDARY
 El - 30 Az - 30
 Minimum Concentration - 10 Suns
 Maximum Concentration - 10058 Suns

Figure 34: Solar flux density in the middle of a SILO secondary element.

Criterion number 3, Refractive index, is a very important system consideration. The higher the refractive index of a glass, the less curvature it needs to produce a given optical power. With less curvature, the lens diameter increases. With a larger diameter, more rays are collected and the allowable tracking error goes up. Figures 35 and 36 show the optics transmission versus tracking error for an f-1.2 300X system designed using three different types of glass for the SILO secondary element. (The refractive index given is measured at the 0.589-micron sodium line.)

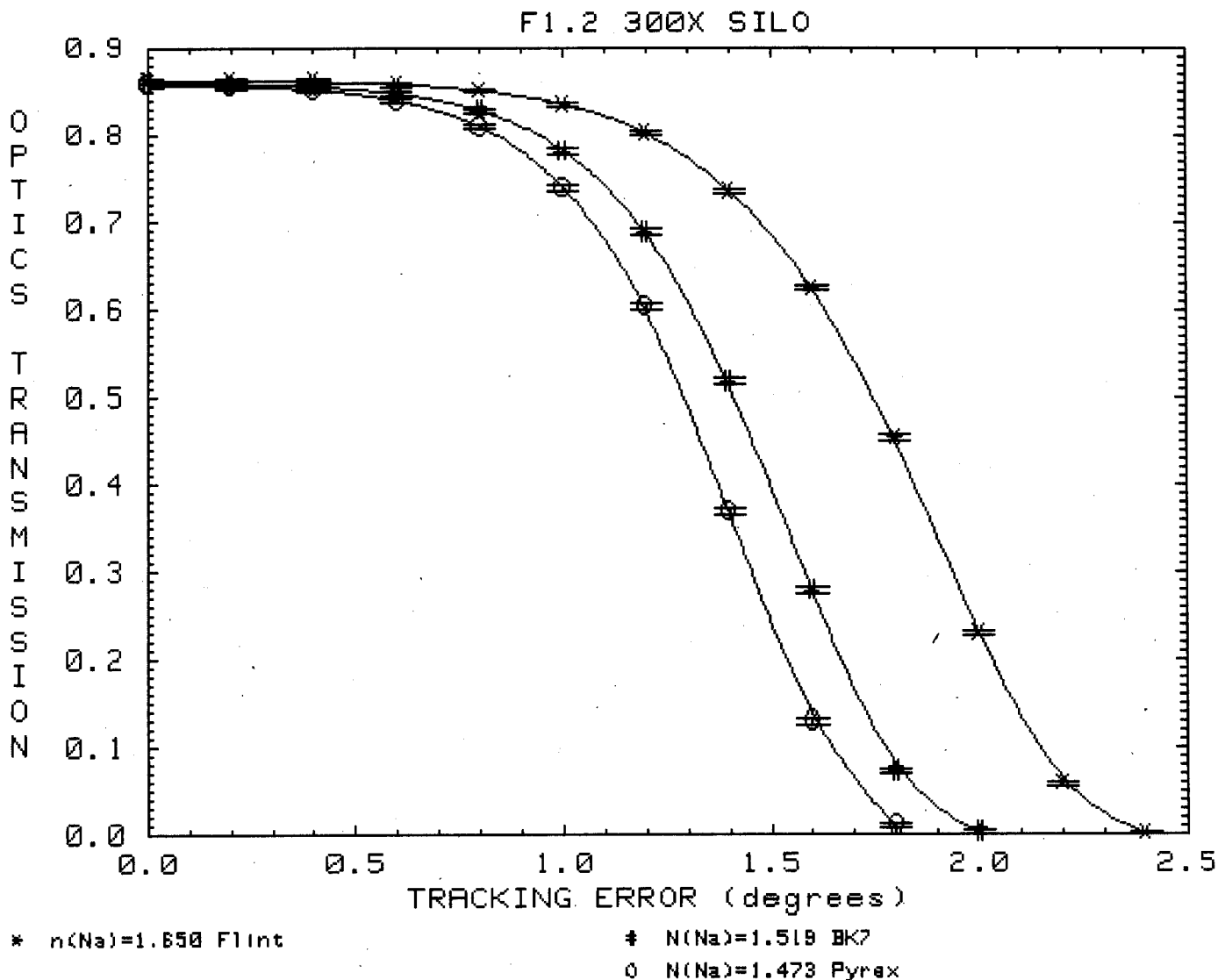


Figure 35: Optics transmission as a function of tracking error for three different glasses.

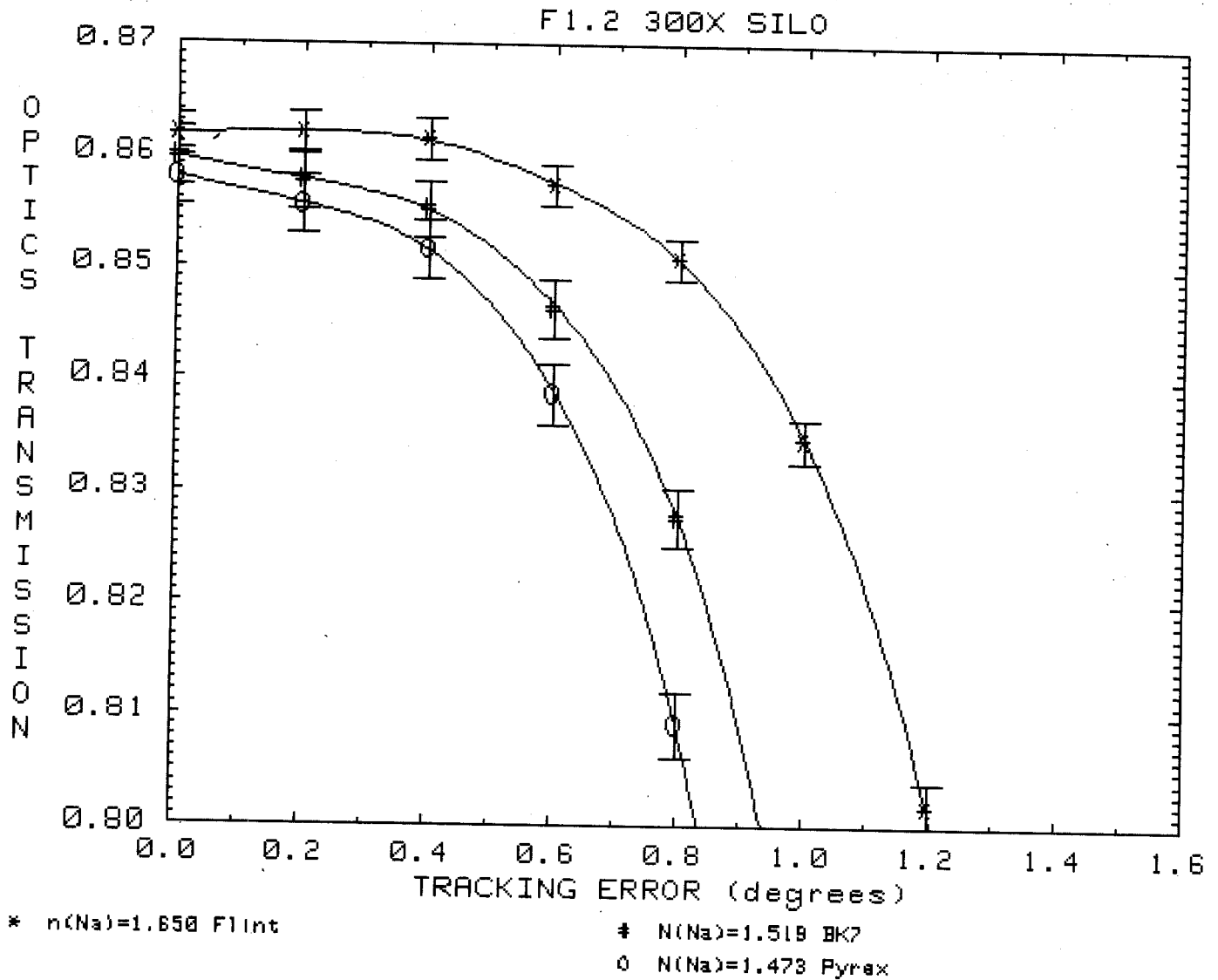


Figure 36: Three different glasses near the 0 tracking error point.

Figure 36 shows the identical curves, but with the vertical axis greatly expanded. Clearly the higher index material is preferred. The difference would be even more pronounced if we were looking at a system with a higher geometric concentration.

Another way to look at the effect of refractive index is to observe that for a given desired allowable tracking-error range; increasing the refractive index of the secondary glass allows a higher concentration ratio and hence a smaller cell.

The optical transmission, criterion 4, of a candidate glass should be very carefully examined over the entire solar spectrum. This optical element is quite thick, and even very small amounts of an element like iron (which gives glass a greenish color and absorbs light in the red and near-infrared) can drastically reduce the optical transmission. Figure 37 shows the optical transmission of the system (as measured by the short-circuit current of a Si cell) as a function of the near-infrared absorption coefficient of a hypothetical glass in an f-1.2 300X SILO secondary.

A typical EGG or SILO secondary is about 5 cm tall. If BK7 glass is used, absorption in the BK7 glass reduces the short-circuit current of a Silicon cell about 0.5%. On the other hand if Pyrex is used, the short-circuit current of a Silicon cell is lowered about 8% by absorption in the Pyrex. Thus a substantial efficiency loss results, as well as significant heating in the glass.

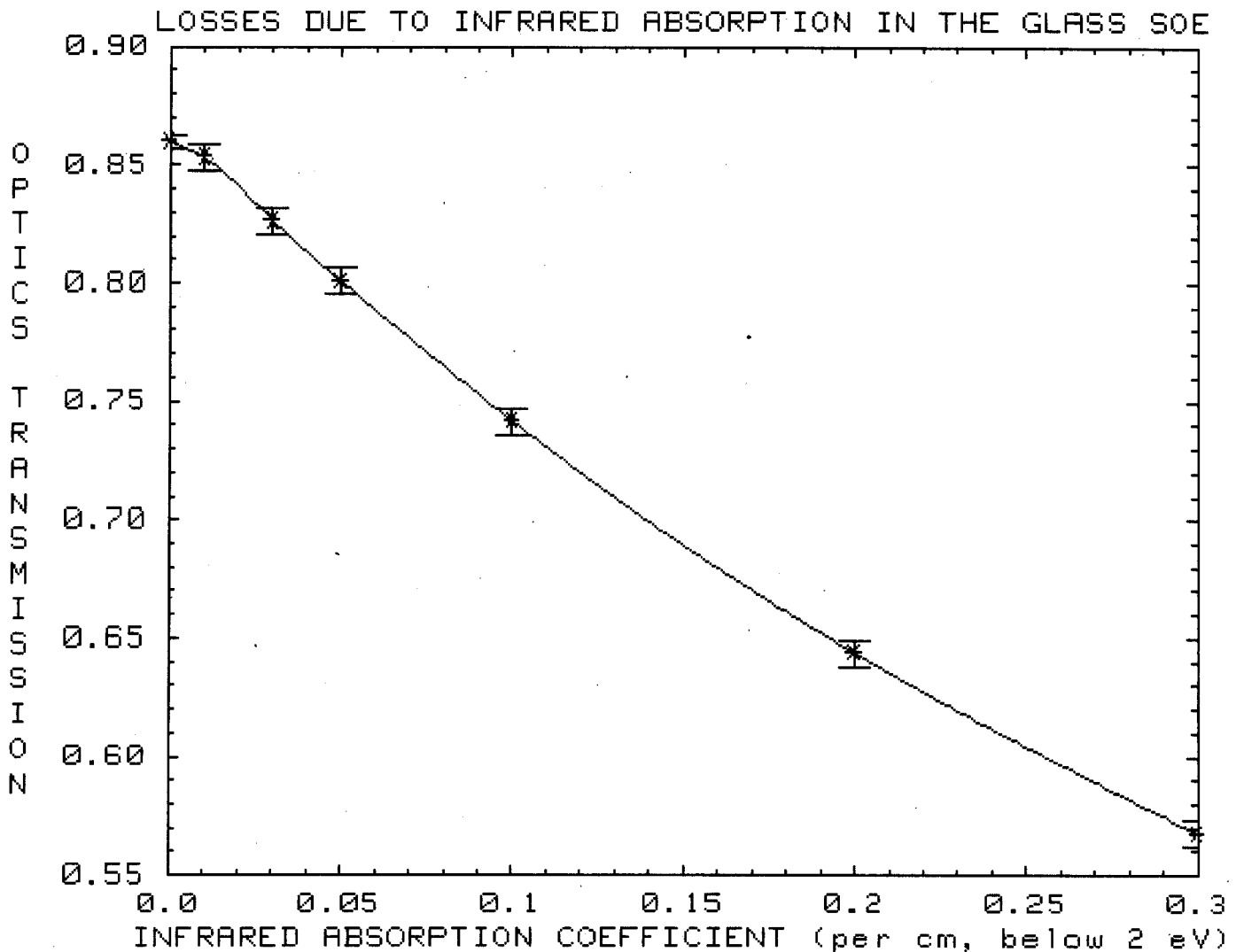


Figure 37: Optical transmission versus secondary glass near-infrared absorption coefficient.

Clearly a candidate glass should have an absorption coefficient below 0.05 per cm across the near-infrared spectrum to be useful in this application. Impurity content can vary drastically from batch to batch on some low-cost glasses, so don't rely on testing one sample, but include absorption coefficient maxima as part of the specification given to a glass manufacturer.

Operation of the SILO Secondary at other than the Focal Point

If you examine Figure 38, which is a repeat of Figure 18, you will notice that the total diameter of the ray bundles decreases toward the center of the secondary. Remember that these rays are shown for a "sun" with an angular diameter 4 times larger than the real sun; hence, rays are shown for all tracking errors (out to about 1.5 degrees) at once. If the secondary were made shorter, the cell could be made smaller and still capture all of the rays. Or, if the cell were kept the same size, the secondary could be made larger and would capture more rays from the primary lens, allowing a larger tracking error range. Taking this approach would, of course, violate the imaging conditions, which gives this secondary many of its worthwhile properties. But, perhaps if the deviation from the exact focal point were small, most of the desired properties would be retained, while still producing an improved error tolerance.

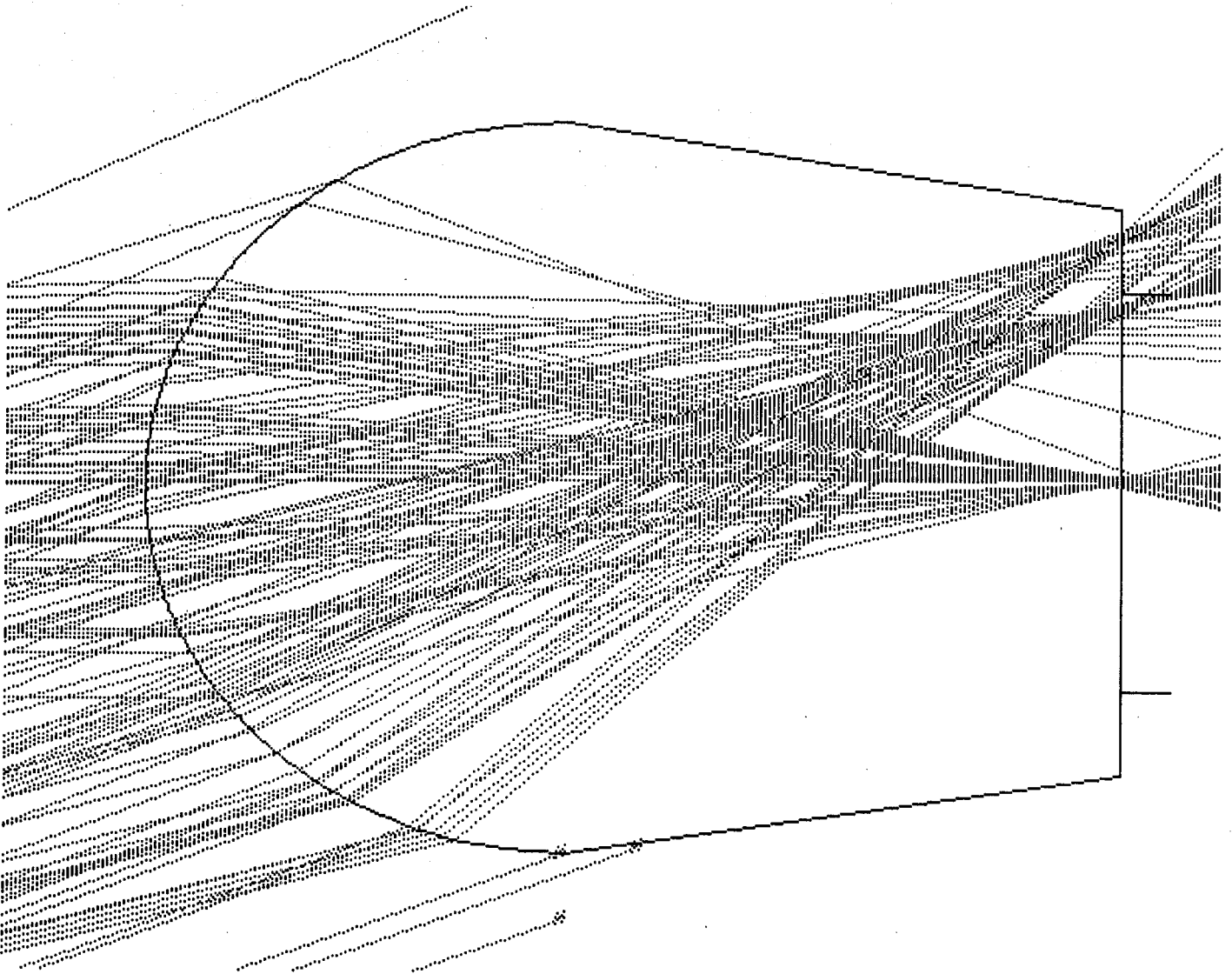


Figure 38: Close-up of a SILO cell assembly showing the imaging properties.

This concept was tested using the computer model. Figure 39 shows a trial design, in which the secondary is enlarged in diameter so that the focal point occurs approximately 0.12 inches below the cell. This results in a 17% increase in the diameter of the secondary.

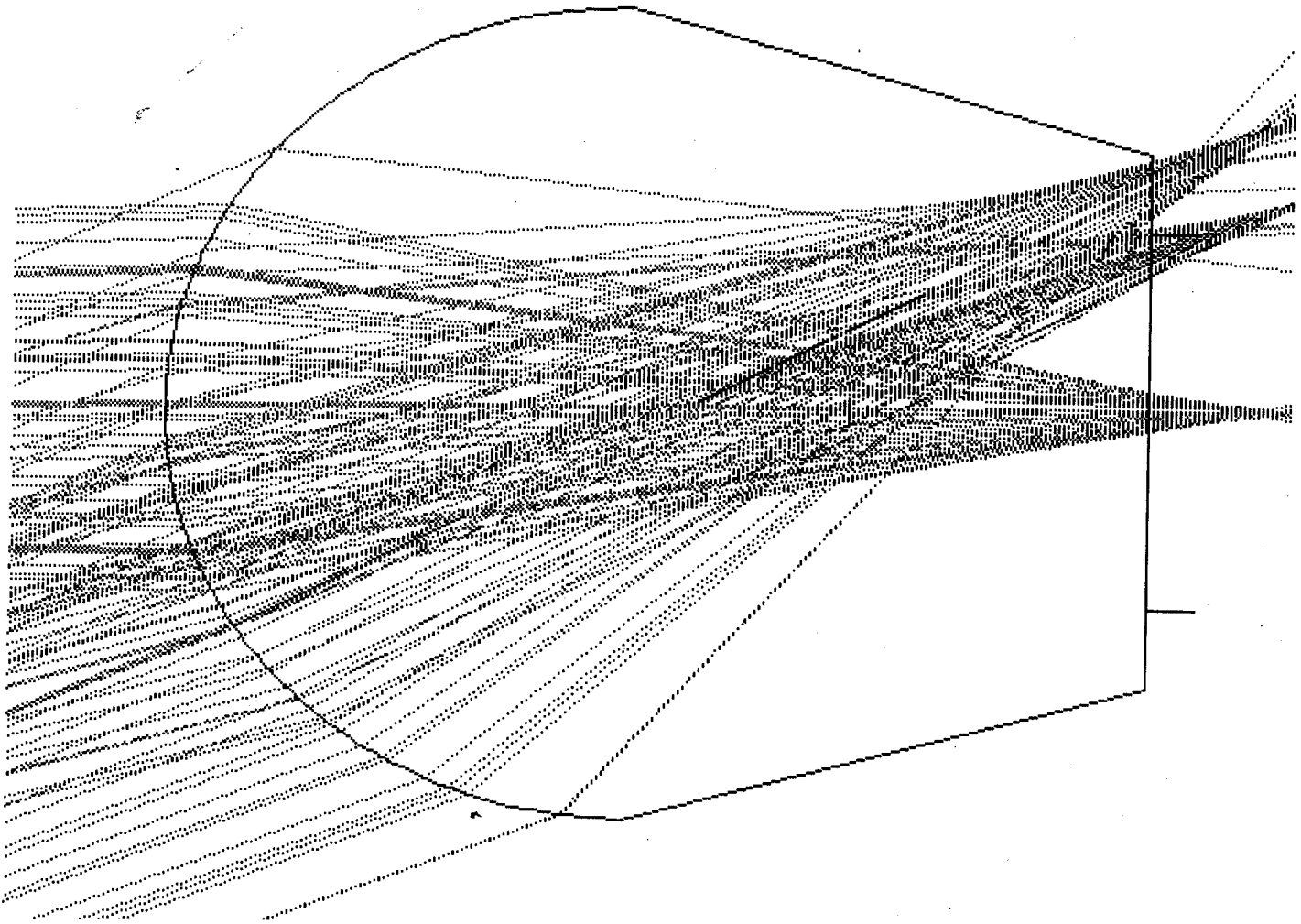


Figure 39: Close-up of a SILO cell assembly with an enlarged secondary.

Figure 40 is a spot diagram, similar to Figure 19, which shows the extent of the spreading of each ray bundle for this system. Each spot on the cell is about 0.044 inches in diameter. Thus we have a situation in which the rays shift about 0.02 inches per degree of tracking error, instead of a nominal shift of 0 under the focus condition. This is still a fairly small shift, and the bundles are still distributed quite uniformly across the cell.

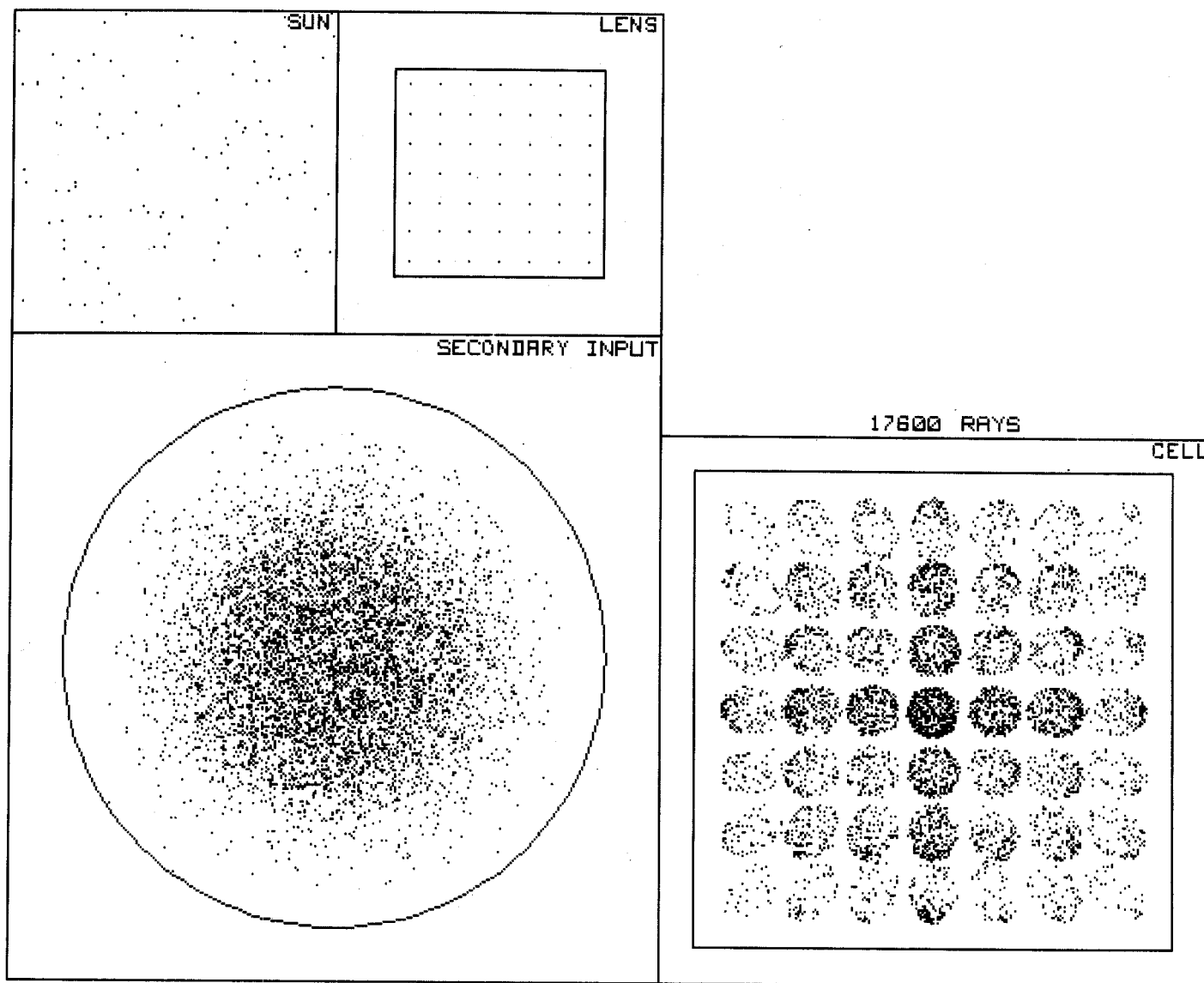
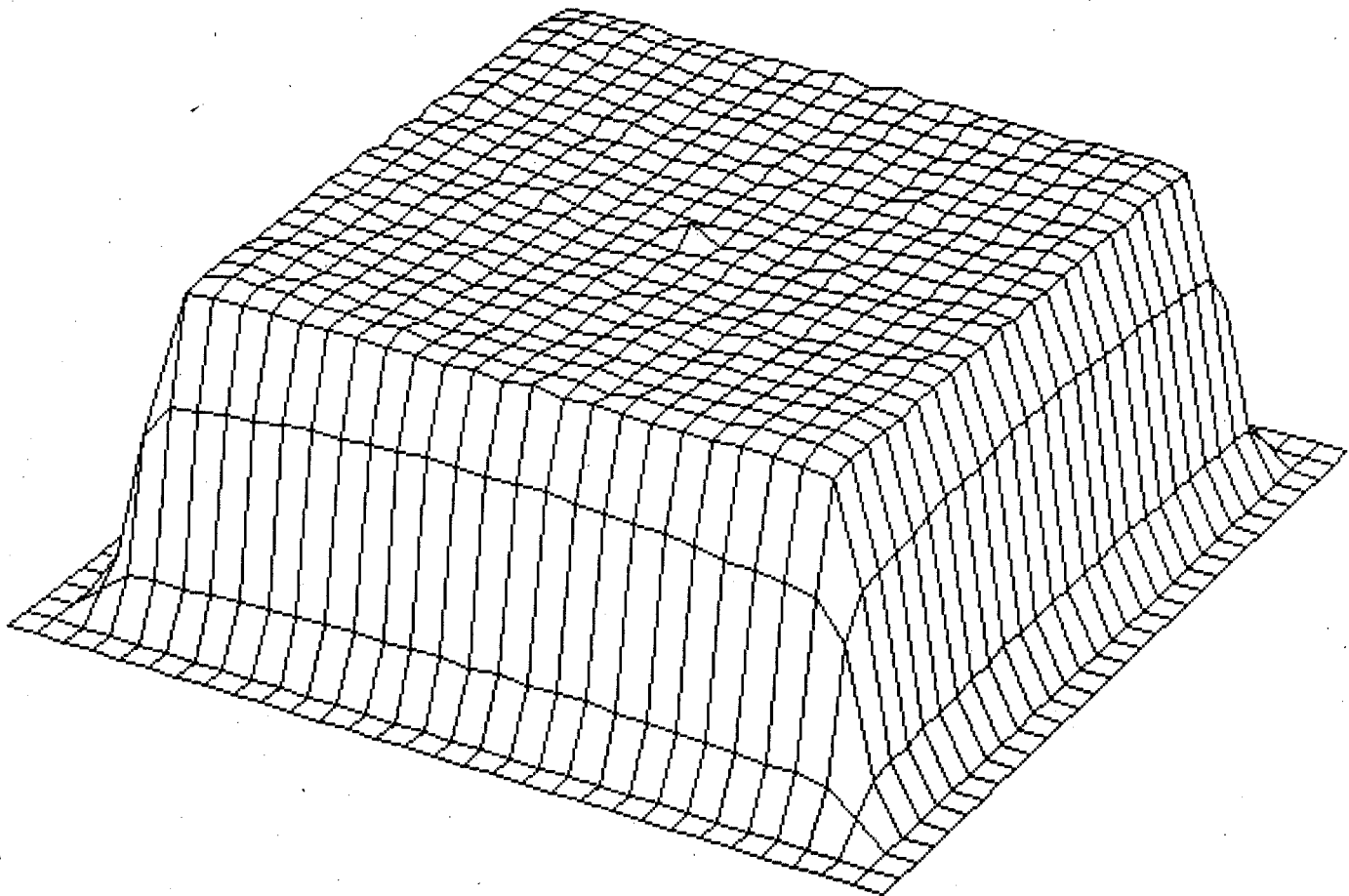


Figure 40: Spot diagram showing the ray bundle size on the cell.

These results looked hopeful, so a full computer run was done to check the actual flux profile and the tracking error tolerances.

The flux uniformity which was obtained is shown in Figure 41. Compared with Figure 20, which is for the in-focus case, the sides are slightly slanted instead of straight up and down, but otherwise the distribution is equally uniform. This distribution should give excellent cell performance.



3-D PLOT OF F1.2 300X BK7 SILO IMAGING POINT BEYOND CELL
 E1 - 30 Az - 30
 Minimum Concentration - 0 Suns
 Maximum Concentration - 318 Suns

Figure 41: Cell short-circuit current flux in the 300X SILO enlarged secondary example.

There is, of course, a limit to how far from the focal point one can go while still maintaining a reasonable flux distribution. Figure 34 showed the distribution near the middle of the secondary. That distribution would not be useable on a cell and would show drastic movement with tracking errors.

The real test of this beyond-focus concept comes in off-track performance. Figure 42 shows clearly the advantage of the larger secondary. The beyond-focus secondary gives an extra 0.3 degree of allowable tracking error.

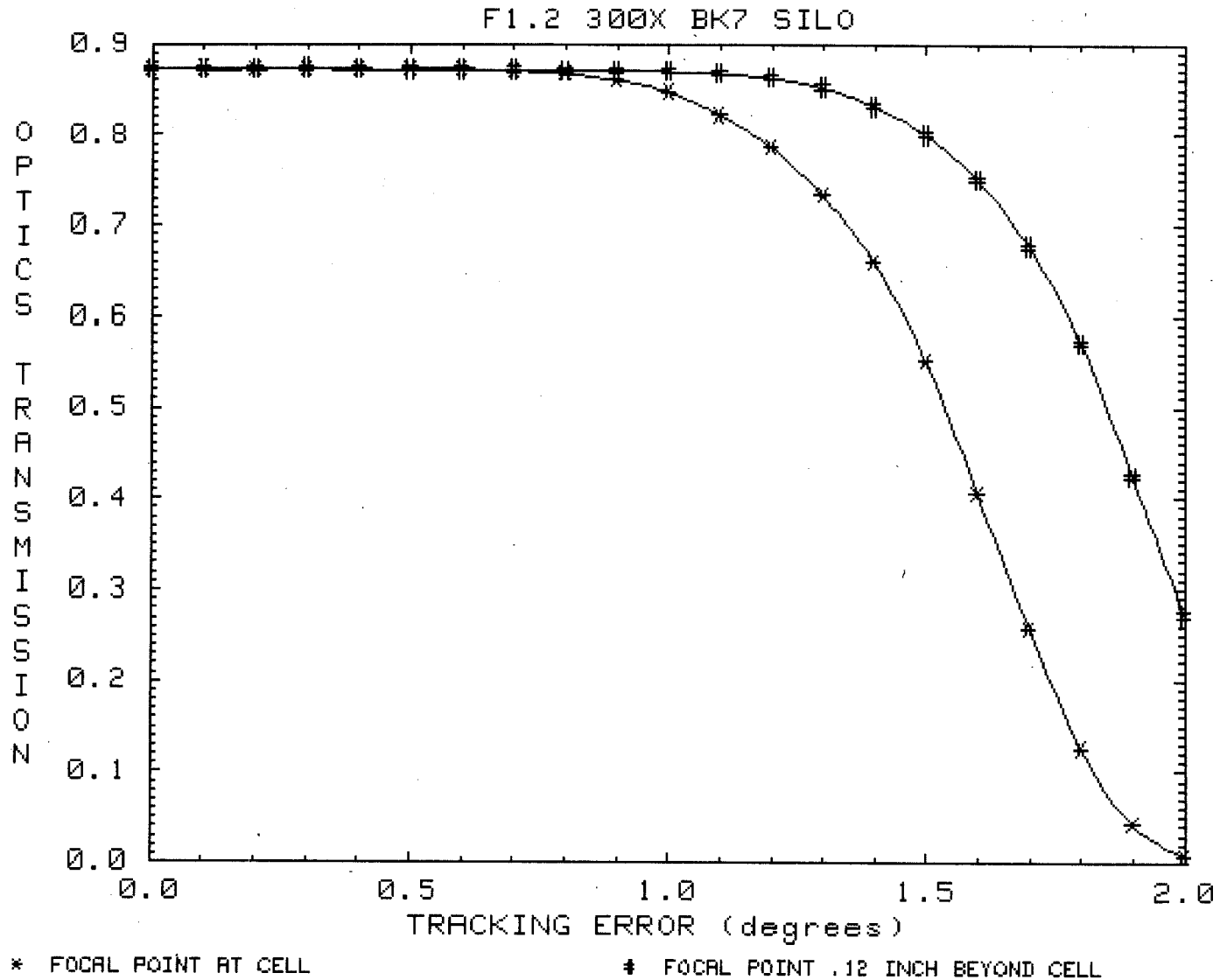


Figure 42: Comparison of an on-focus to a beyond-focus SILO secondary.

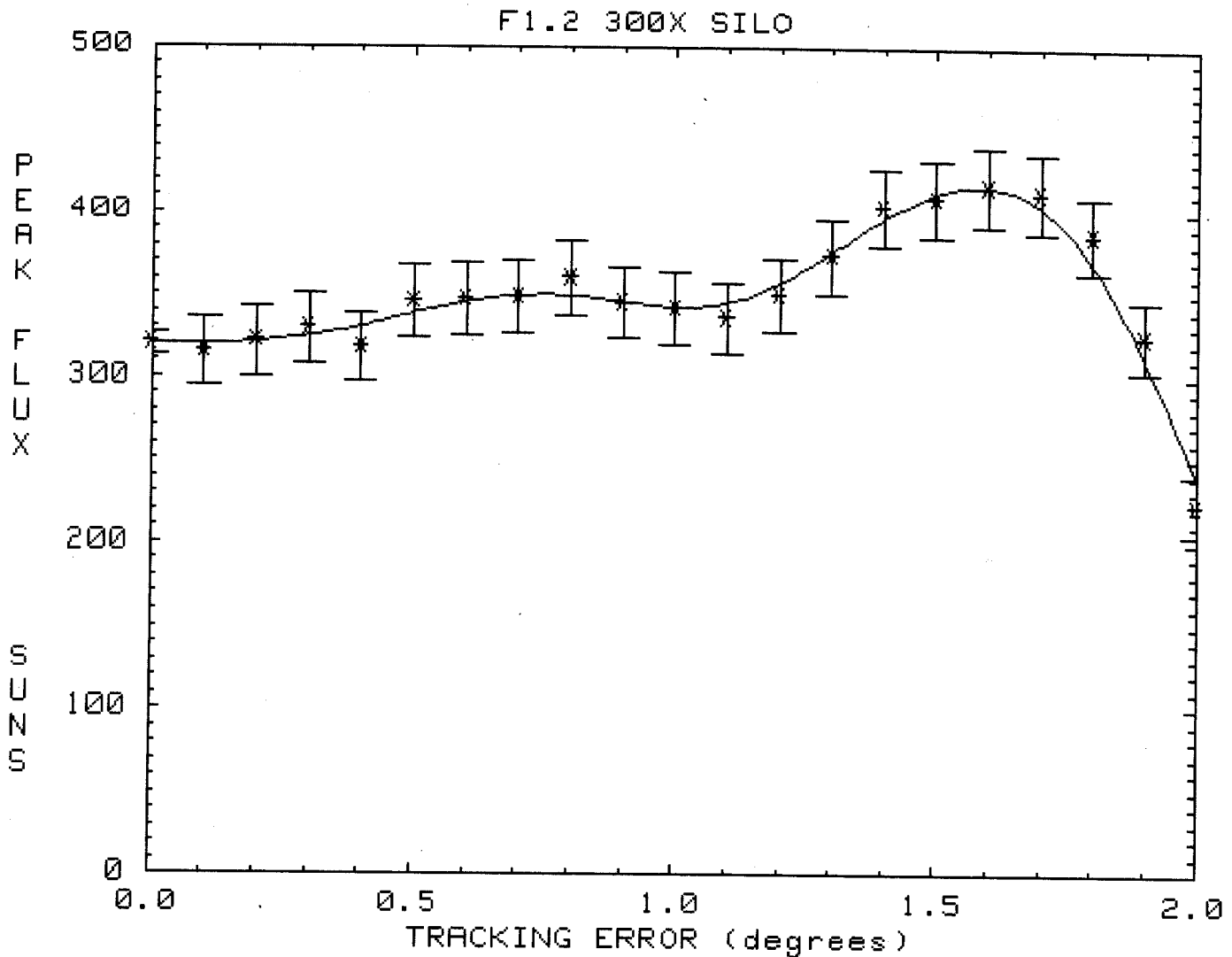


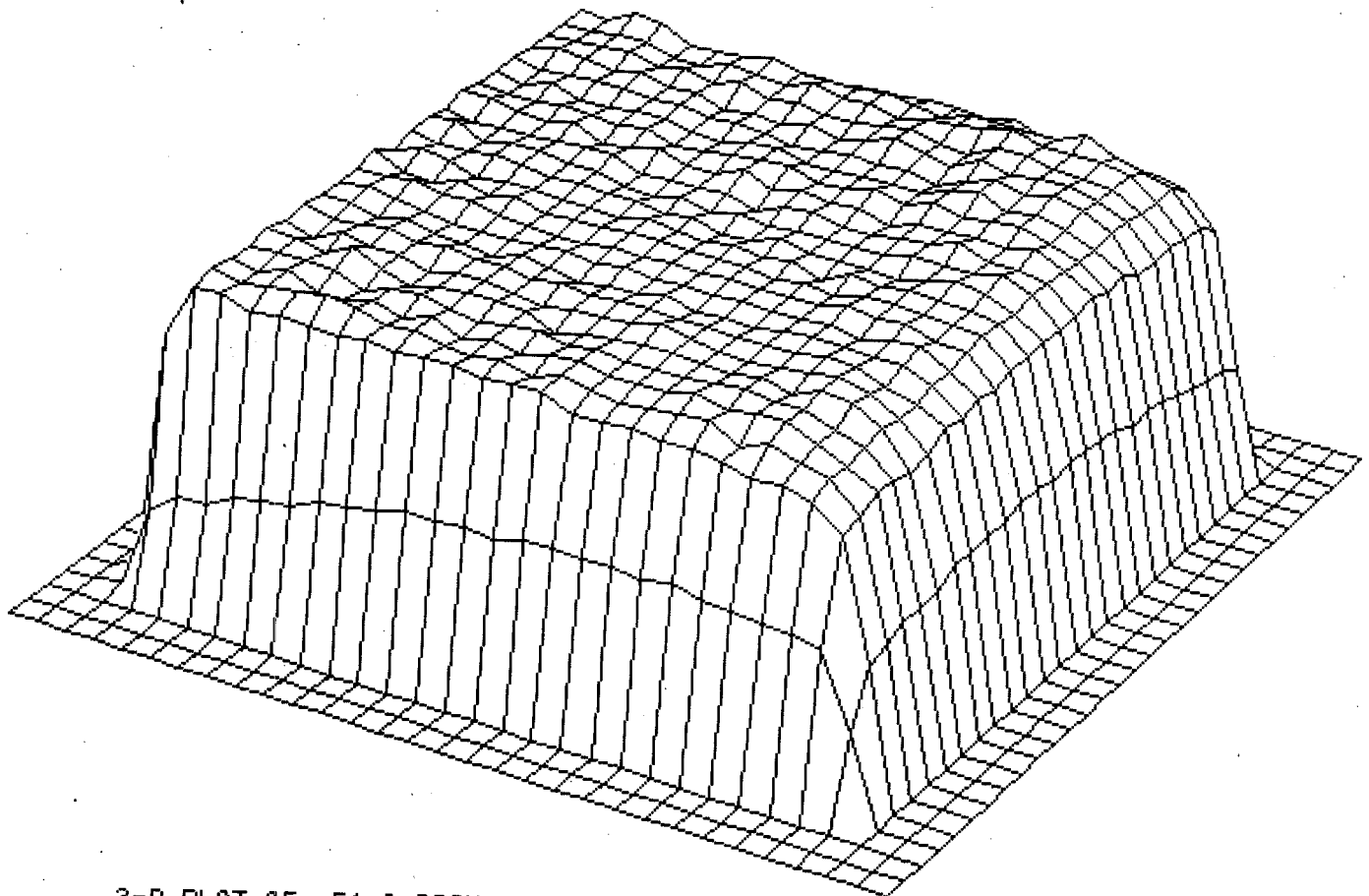
Figure 43: Peak solar flux (short-circuit current weighted) of the beyond-focus optical system versus tracking error.

Figure 43 shows that the flux profile remains extremely uniform over the extended tracking error range. Comparing this profile with that of Figure 23 shows that the peak flux as a function of tracking error behaves almost identically to the on-focus case.

There are two important conclusions resulting from these observations. First, the tolerances on the secondary height need not be as tight as one might first infer from the need to maintain focusing. This may be important in a low-cost molding operation. Second, in doing an overall system design, the beyond-focus case should be carefully examined.

Conclusions

There is no doubt that this double-imaging optics system is an elegant and straightforward method for designing PV optical systems. This system makes design and optimization of the optics straightforward, replacing the mixture of art and science that normally goes into a solar optical design. It results in wider tolerances to all kinds of mounting and pointing errors than any other known design, maintaining high optical transmission values and extremely uniform solar flux profiles over very reasonable manufacturing and tracking tolerances. Figure 44 shows the flux uniformity when operating the f-1.2 300X SILO system with a 0.1-inch mounting error in the lens-to-cell spacing, a 0.1-inch mounting error in the cell plane (the cell assembly is not positioned directly under the lens), and a 0.25-degree tracking error (in a direction orthogonal to the cell mounting error). In this figure the SILO has an ideal AR coating applied. The transmission is down less than 0.1% from the value with everything aligned perfectly, and the flux profile is still uniform. No other known concentrator system performs this well. The SILO optical system is worth serious consideration for new concentrator optical designs. The major potential drawback for the SILO, that must be taken into account for cost effective designs, is the cost of the AR coating or the reflection loss at the air-to-SILO interface which results from its omission.



3-D PLOT OF F1.2 300X SILO with TRACKING and MOUNTING ERRORS
 E1 = 30 Az = 30
 Minimum Concentration = 0 Suns
 Maximum Concentration = 341 Suns

Figure 44: Flux uniformity under a combination of error conditions.

In the process of performing this work, computer ray trace and primary/secondary lens design programs were developed that allow the user to design and evaluate both lenses (with either an EGG or a SILO secondary) for a particular application. Many of the figures in this report were generated by these programs. These programs are available from James Associates for HP 9000 and PC computers.

DISTRIBUTION LIST

Acrian
Attn: Mary Bernstein
490 Race Street
San Jose, CA 95126

AESI
Attn: William J. Todorof
1001 W. 17th Street, Unit J
Costa Mesa, CA 92627

Alpha Solarco (2)
Attn: Edward Schmidt
Don Carroll
600 Vine Street, Suite 608
Cincinnati, OH 45202

Alternative Sources of Energy
Attn: Larry Stoiaken
107 S. Central Avenue
Milaca, MN 56353

American Optical Corporation (2)
Attn: Clark Grendol
R. F. Woodcock
14 Mechanic Street
Southbridge, MA 01550

Applied Solar Energy Corp (3)
Attn: Charlie Chu
Dave Kozak
Ken Ling
15251 E. Don Julian Road
City of Industry, CA 91746

ARCO Solar, Inc. (2)
Attn: Charles Gay
Kim Mitchell
P. O. Box 6032
Camarillo, CA 93010

Arizona Public Service Company
Attn: Tom Lepley
P. O. Box 53999
Mail Station 3875
Phoenix, AZ 85072-3999

Arizona State University (2)
College of Engineering and
Applied Science
Attn: Charles Backus
G. Schwuttke
Tempe, AZ 85287

Astropower Division (2)
Attn: A. Barnett
R. Hall
30 Lovett Avenue
Newark, DE 19711

Raymond J. Bahm and Associates
Attn: Raymond J. Bahm
2513 Kimberley Ct., NW
Albuquerque, NM 87120

Bechtel National, Inc.
Attn: Walter J. Stolte
Mail Stop 50/15/D17
P. O. Box 3965
San Francisco, CA 94119

Black & Veatch
Attn: Sheldon L. Levy
P. O. Box 8405
Kansas City, MO 64114

Boeing Electronics Company
Attn: Lewis Fraas
P. O. Box 24969, MS 9Z-80
Seattle, WA 98124-6269

Cagle and Associates, Inc.
Attn: Mr. Carroll Cagle
P. O. Drawer 1926
Albuquerque, NM 87103

California Institute of
Technology
Electrical Engineering Dept.
Attn: Marc A. Nicolet
116-81
Pasadena, CA 91125

City of Austin
Electric Dept.
Attn: John E. Hoffner
P. O. Box 1088
Austin, TX 78767

Commission of the
European Communities
Attn: Wolfgang Palz
200 Rue de la Loi
1049 Brussels, Belgium

Crystal Systems, Inc.
Attn: Frederick Schmid
27 Congress Street
Salem, PA 01970

Delta Solar
Attn: Leon Wahler
1148 W. Fremont
Stockton, CA 95203

ENEA
Attn: Renato Gislon
Departiment FARE
Divisione Tecnologie Fotovoltaiche
C.R.E. Casaccia
00060 S. M. Galeria
Roma, Italy

Energy, Mines and Resources
Canada
Energy Efficiency Branch
Attn: J. E. Smith, Rm 1133
460 O'Connor Street
Ottawa, Ontario
Canada K1A 0E4

Electric Power Research Inst. (2)
Attn: Frank Goodman
Ed DeMeo
3412 Hillview Avenue
P. O. Box 10412
Palo Alto, CA 94303

ENTECH (2)
Attn: Walter Hess
Mark O'Neill
P. O. Box 612246
DFW Airport, TX 75261

Max Findel
836 Rio Arriba Avenue, SE
Albuquerque, NM 87123

Fraunhofer Institute for
Solar Energy Systems (FhG-ISE)
Attn: A. Goetzberger
Oltmannsstr. 22
D-7800 Freiburg
West Germany

Fresnel Optics, Inc. (2)
Attn: Helmut Walter
John Eggar
1300 Mt. Read Blvd.
Rochester, NY 14606

Gas Research Institute
Attn: Dr. Ab Flowers
8600 West Bryn Mawr Avenue
Chicago, IL 60631

General Dynamics/Space Systems
Attn: Ted Stearn
Mail Zone 24-8730
P. O. Box 85990
San Diego, CA 92138

Georgia Institute of Technology
School of Electrical Engineering
Attn: Professor Aject Rohatgi
Atlanta, GA 30331

Heliopower, Inc.
Attn: Joel Davidson
P. O. Box 5089
Culver City, CA 90231

Heliotrak (2)
Attn: Jonathan Frey
Anthony Morris
13566 Tomki Road
Redwood Valley, CA 94570

High Intensity Photovoltaics, Inc.
Attn: Bernard L. Sater
9007 Westlawn Blvd.
Olmsted Falls, OH 44138

Hughes Research Labs (2)
Attn: S. Kamath
R. Loo
3011 Malibu Canyon Road
Malibu, CA 90265

Institute of Advanced
Manufacturing Sciences, Inc.
Attn: Paul R. Warndorf
1111 Edison Drive
Cincinnati, OH 45216

Instituto de Energia Solar (2)
Ciudad Universitaria, S/N
Attn: Antonio Luque
Gabriel Sala
E.T.S.I. Telecomunicacion (UPM)
28040 - Madrid
Spain

Intersol Power Corporation
Attn: John Sanders
11901 West Cedar
Lakewood, CO 80228

James Associates (10)
Attn: Larry James
1525 E. County Road 58
Fort Collins, CO 80524

Jet Propulsion Laboratory
Attn: Ron Ross
R. S. Sugimura
4800 Oak Grove Drive
Pasadena, CA 91109

Kopin Corporation
Attn: M. Spitzer
695 Myles Standish Blvd.
Taunton, MA 02780

Luz Engineering Corp.
Attn: David Kearny
924 Westwood Blvd., Suite 1000
Los Angeles, CA 90024

M/A-COM PHI (2)
Attn: Sewang Yoon
Jeff Meyer
1742 Crenshaw Blvd.
Torrance, CA 90501

MAKO Enterprises, Inc.
Attn: Ken Stone
6882 Via Angelina
Huntington Beach, CA 92647

Midway Lab
Attn: Paul Collard
2255 East 75th Street
Chicago, IL 60649

MIT/Lincoln Lab
Attn: George Turner
Box 73
Lexington, MA 02173

Mobil Solar Energy Corporation
Attn: Juris Kalejs
4 Suburban Park Drive
Billerica, MA 01821

New Mexico State University (2)
Attn: L. Matthews
G. Mulholland
P. O. Box 3450
Las Cruces, NM 88003

NYSERDA
Attn: Burton Krakow
2 Rockefeller Plaza
Albany, NY 12223

Oak Ridge National Laboratory (2)
Attn: R. F. Wood
R. D. Westbrook
P. O. Box Y
Oak Ridge, TN 37830

Ohara Corporation
Attn: B. D. Hoffman
215 Ave. Del Mar, Suite L
San Clemente, CA 92672

Ohio State University
Welding Department
Attn: Charles Albright
190 West 19th Street
Columbus, OH 43210

Pacific Gas & Electric (2)
Attn: Steve Hester
Kay Firor
3400 Crow Canyon Road
San Ramon, CA 94583

Photics, Inc.
Attn: Jacques Ludman
76 Treble cove Road
North Billerica, MA 01862

Public Service Company
of New Mexico
Attn: R. Frank Burcham
Alvarado Square, MS 0150
Albuquerque, NM 87158

Purdue University
Attn: Richard Schwartz
School of Electrical Engineering
West Lafayette, IN 47907

Sci-Tech International
Attn: Ugur Ortabasi
5673 W. Las Positas Blvd.
Suite 205
Pleasanton, CA 94566

SERA Solar Corporation
Attn: James Gibbons
3151 Jay Street
Santa Clara, CA 95054

SERI (4)
Attn: J. Benner
B. Sopor
T. Surek
E. Witt
1617 Cole Blvd.
Golden, CO 80401

SERI Library
1617 Cole Blvd.
Golden, CO 80401

Solar Engineering
Applications Corporation
Attn: Donald Curchod
2030 Fortune Drive
San Jose, CA 95131

Solarex Aerospace Division (2)
Attn: Jerry Silver
Ramon Dominguez
201 Perry Parkway, Suite 1
Gaithersburg, MD 20877

Solarex Corporation
Attn: J. Wohlgemuth
630 Solarex Court
Frederick, MD 20701

SOLEC International, Inc.
Attn: Ishaq Shahryar
12533 Chadron Avenue
Hawthorne, CA 90250

Southern California Edison
Attn: Nick Patapoff
2244 Walnut Grove Avenue
Rosemead, CA 91770

SPECO
Attn: Walt Hart
P. O. Box 91
Morrison, CO 80465

Spectrolab
Attn: D. Lillington
12500 Gladstone Avenue
Sylmar, CA 91342

Spire Corporation (2)
Attn: M. J. Nowlan
S. Tobin
Patriots Park
Bedford, MA 01730
Springborn Laboratories, Inc.
Attn: Bernard Baun
Enfield, CT 06082

Stanford University (2)
Attn: Richard Swanson
Ron Sinton
McCullough 206
Stanford, CA 94305

Stillpoint Solar
Attn: John Lyle
P. O. Box 929
Manitou Springs, CO 80821

Strategies Unlimited
Attn: Robert O. Johnson
201 San Antonio Circle
Suite 205
Mountain View, CA 94040

3M Company (3)
Solar Optical Products
Attn: Sanford Cobb, 235-BC-05
Paul Jaster, 225-2N-06
Al Zderad, 235, BC-05

3M Center
St. Paul, MN 55144

U. S. Department of Energy
Albuquerque, Operations Office
Attn: Dean Graves
P. O. Box 5400
Albuquerque, NM 87115

U. S. Department of Energy (5)
Attn: Robert Annan
Morton Prince
Andrew Krantz
Lloyd Herwig
Richard King
1000 Independence Avenue, SW
Washington, DC 20585

University of Arizona
Solar & Energy Research Facility
Attn: D. E. Osborn
CE Bldg. #76
Tucson, AZ 85721

University of Chicago
Attn: Joseph O'Gallagher
5640 South Ellis Avenue
Chicago, IL 60637

University of New Mexico/NMERI
Attn: G. Leigh
Campus Box 25
Albuquerque, NM 87131

Varian Associates (2)
Attn: N. Kaminar
G. Virshup
611 Hansen Way, MS K-124
Palo Alto, CA 94303

Wattsun
Attn: John Doherty
P. O. Box 751
Albuquerque, NM 87103

Westinghouse Electric Corporation
Attn: Charles Rose
P. O. Box 10864
Pittsburgh, PA 15236

Wirtschaft Und Infrastruktur
GMBH & Co
Planungs-KG
Attn: Matthew S. Imamura
Sylvensteinstrasse 2
D-8000 Munchen 70
West Germany

Wright Patterson AFB
Attn: Jack Geis
AFWAL/POOC
Wright Patterson AFB, OH

1810	R. G. Kepler
1811	C. L. Renschler
1811	L. Salgado
1812	R. A. Assink
1820	J. B. Woodard
1830	M. J. Davis
1840	R. E. Loehman
6000	D. L. Hartley
6200	V. L. Dugan
6220	D. G. Schueler
6221	E. C. Boes
6221	J. E. Cannon
6221	J. L. Chamberlin
6221	C. J. Chiang
6221	A. B. Maish
6221	E. H. Richards
6221	C. B. Stillwell (10)
6223	G. J. Jones
6224	D. G. Schueler, Actg
6224	A. R. Mahoney
6224	H. L. Tardy
8524	J. A. Wackerly
3141	S. A. Landenberger (5)
3154-1	C. L. Ward For DOE/OSTI (8)
3151	W. I. Klein (3)



8232-2/069226



00000001 -



8232-2/069226



00000001 -



8232-2/069226



00000001 -